J. Fluid Mech. (1987), *vol.* 177, *pp.* 133–166
Printed in Great Britain

Turbulence statistics in fully developed channel flow at low Reynolds number

By JOHN KIM, PARVIZ MOIN AND ROBERT MOSER
NASA Ames Research Center, Moffett Field, CA 94035, USA

(Received 19 February 1986)

A direct numerical simulation of a turbulent channel flow is performed. The unsteady Navier–Stokes equations are solved numerically at a Reynolds number of 3300, based on the mean centreline velocity and channel half-width, with about 4×10^6 grid points ($192 \times 129 \times 160$ in x, y, z). All essential turbulence scales are resolved on the computational grid and no subgrid model is used. A large number of turbulence statistics are computed and compared with the existing experimental data at comparable Reynolds numbers. Agreements as well as discrepancies are discussed in detail. Particular attention is given to the behaviour of turbulence correlations near the wall. In addition, a number of statistical correlations which are complementary to the existing experimental data are reported for the first time.

1. Introduction

Fully developed channel flow has been studied extensively to increase the understanding of the mechanics of wall-bounded turbulent flows. Its geometric simplicity is attractive for both experimental and theoretical investigations of complex turbulence interactions near a wall. As a result, a large number of experimental and computational studies of channel flow have been carried out.

Nikuradse (1929) and Reichardt (1938) were among the first to investigate fully developed turbulent channel flow. Nikuradse's measurements were limited to the mean flow; Reichardt reported velocity fluctuations in the streamwise and normal (to the wall) directions. Laufer (1951) was the first to document detailed turbulence statistics. His measurements were made at three Reynolds numbers (12300, 30800, and 61600), based on the mean centreline velocity and the channel half-width. Comte-Bellot (1963) provided the most extensive data, including many higher-order statistics such as two-point correlations, energy spectra, skewness and flatness factors. Her measurements were made over the Reynolds-number range 57000–230000. Clark (1968) reported additional detailed information in the regions very near the wall over the Reynolds-number range 15000–45600. Hussain & Reynolds (1975) conducted experiments in an extremely long, two-dimensional channel to confirm that the higher-order turbulence statistics reached a fully developed state. The ratio of their channel length to the channel half-width was about 450, compared with 86, 122 and 120 of Laufer, Comte-Bellot and Clark, respectively. The Reynolds-number range in the experiment of Hussain & Reynolds was 13800–33300. Eckelmann (1970) carried out his experiment with oil as the working fluid, and at very low Reynolds numbers, 2800 and 4100, to facilitate measurements in the region very close to the wall. Detailed information regarding the turbulence structures near the wall in the same facility were also reported by Eckelmann (1974) and Kreplin & Eckelmann (1979). Johansson & Alfredsson (1982) presented recent measurements at a Reynolds-number range of 6900–24450.

Despite the significant effort in this relative simple flow, there is poor agreement among the reported measurements, even in lower-order statistics such as turbulence intensities, especially in the vicinity of the wall. Part of the discrepancy may be due to the wide range of Reynolds numbers used in the experiments – for example, it is well known that there is a significant Reynolds-number effect on the log law of mean velocity profiles – but most of the scatter is probably a result of experimental uncertainty involved in measuring turbulence quantities near the wall, where the presence of high shear and small scales of turbulent motions makes measurements extremely difficult. Johansson & Alfredsson (1984) reported the effect on turbulence measurements of imperfect spatial resolution due to probe length. The low-Reynolds-number experiments in the oil channel by Eckelmann and his colleagues at Göttingen attempted to reduce this difficulty by making the wall layer thick enough to allow reliable measurements in this region.

In recent years, numerical simulations of turbulent flows have become an important research tool in studying the basic physics of turbulence. For the reasons outlined above, extensive effort has been devoted to the calculation of turbulent channel flow. The simulation databases, which contain three-dimensional velocity and pressure fields, provide information to complement experimental data in the study of the physics of turbulent flows. Interested readers are referred to a recent review article by Rogallo & Moin (1984). Deardorff (1970) and Schumann (1973) performed three-dimensional computations of turbulent channel flow in which synthetic boundary conditions are used in the log layer, rather than the natural no-slip boundary condition, thereby avoiding explicit computation of the near-wall region. Nevertheless, they were able to predict several features of turbulent channel flow with a moderate number of grid points. In the computations of Moin & Kim (1982), the wall region was explicitly computed rather than modelled, and most of the experimentally observed wall-layer structures were reproduced. The database from that simulation has been used extensively for studying the structure of wall-bounded turbulent flows, although the computational resolution was not adequate to completely resolve turbulence scales in the vicinity of the wall. The qualitative statistical and time-dependent features of the flow were in accordance with experimental measurements, but the scales of the flow structures in the wall region were generally larger than the experimental observations. Therefore, reliable quantitative information on turbulence structures could not be extracted from the computations.

The objective of this work is to perform a direct numerical simulation of turbulent channel flow where all essential scales of motion are resolved. The database generated by such a simulation is of considerable value for the quantitative and qualitative studies of the structure of turbulence in wall-bounded flows, and for the design and testing of turbulence closure models. The computed flow fields can also be used to calibrate new measurement techniques that can be used in more complex flows which are currently inaccesible for direct numerical simulations. In this paper we report the results of this simulation, and document its detailed turbulence statistics. The computed results are compared extensively with the available experimental data. Agreements as well as discrepancies will be discussed in detail. In addition, a number of statistical correlations, which complement the existing experimental data, are reported for the first time.

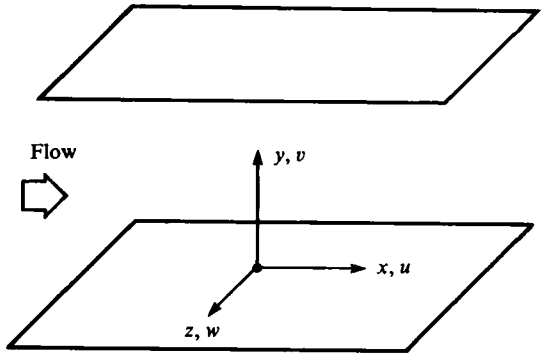

FIGURE 1. Coordinate system in channel.

2. Computational domain and grid spacing

The flow geometry and the coordinate system are shown in figure 1. Fully developed turbulent channel flow is homogeneous in the streamwise and spanwise directions, and periodic boundary conditions are used in these directions. The use of periodic boundary conditions in the homogeneous directions can be justified if the computational box (period) is chosen to include the largest eddies in the flow. As in Moin & Kim (1982), the initial choice of the computational domain is made by examining the experimental two-point correlation measurements. The computational domain is adjusted, if necessary, to assure that the turbulence fluctuations are uncorrelated at a separation of one half-period in the homogeneous directions. The computation is carried out with 3962880 grid points ($192 \times 129 \times 160$, in x, y, z) for a Reynolds number of 3300, which is based on the mean centreline velocity U_c and the channel half-width δ (a Reynolds number of 180 based on the wall shear velocity u_τ). For the Reynolds number considered here, the streamwise and spanwise computational periods are chosen to be $4\pi\delta$ and $2\pi\delta$, respectively (2300 and 1150 in wall units). With this computational domain, the grid spacings in the streamwise and spanwise directions are respectively $\Delta x^+ \approx 12$ and $\Delta z^+ \approx 7$ in wall units.† Non-uniform meshes are used in the normal direction with $y_j = \cos\theta_j$ for $\theta_j = (j-1)\pi/(N-1), j = 1, 2, \ldots, N$. Here N is the number of grid points in the y-direction. The first mesh point away from the wall is at $y^+ \approx 0.05$, and the maximum spacing (at the centreline of the channel) is 4.4 wall units. No subgrid-scale model is used in the computation, since it is shown (Moser & Moin 1984) and confirmed, *a posteriori*, that the grid resolution is sufficiently fine to resolve the essential turbulent scales, even though it is larger than the estimated Kolmogorov scale of 2 wall units obtained using the average dissipation rate per unit mass across the channel width.

Examples of two-point correlations and energy spectra are shown in figures 2 and 3 to illustrate the adequacy of the computational domain and the grid resolutions. In figure 3, k_x and k_z are the wavenumbers in the streamwise and spanwise directions, respectively. In figure 2, the two-point correlations in the x- and z-directions at two y-locations – one very close to the wall and the other close to the centreline – show that they fall off to zero values for large separations, indicating that the computational domain is sufficiently large. The energy spectra shown in figure 3 illustrate that the grid resolution is adequate, since the energy density associated with the high

† The superscript + indicates a non-dimensional quantity scaled by the wall variables; e.g. $y^+ = yu_\tau/\nu$, where ν is the kinematic viscosity and $u_\tau = (\tau_w/\rho)^{\frac{1}{2}}$ is the wall shear velocity.

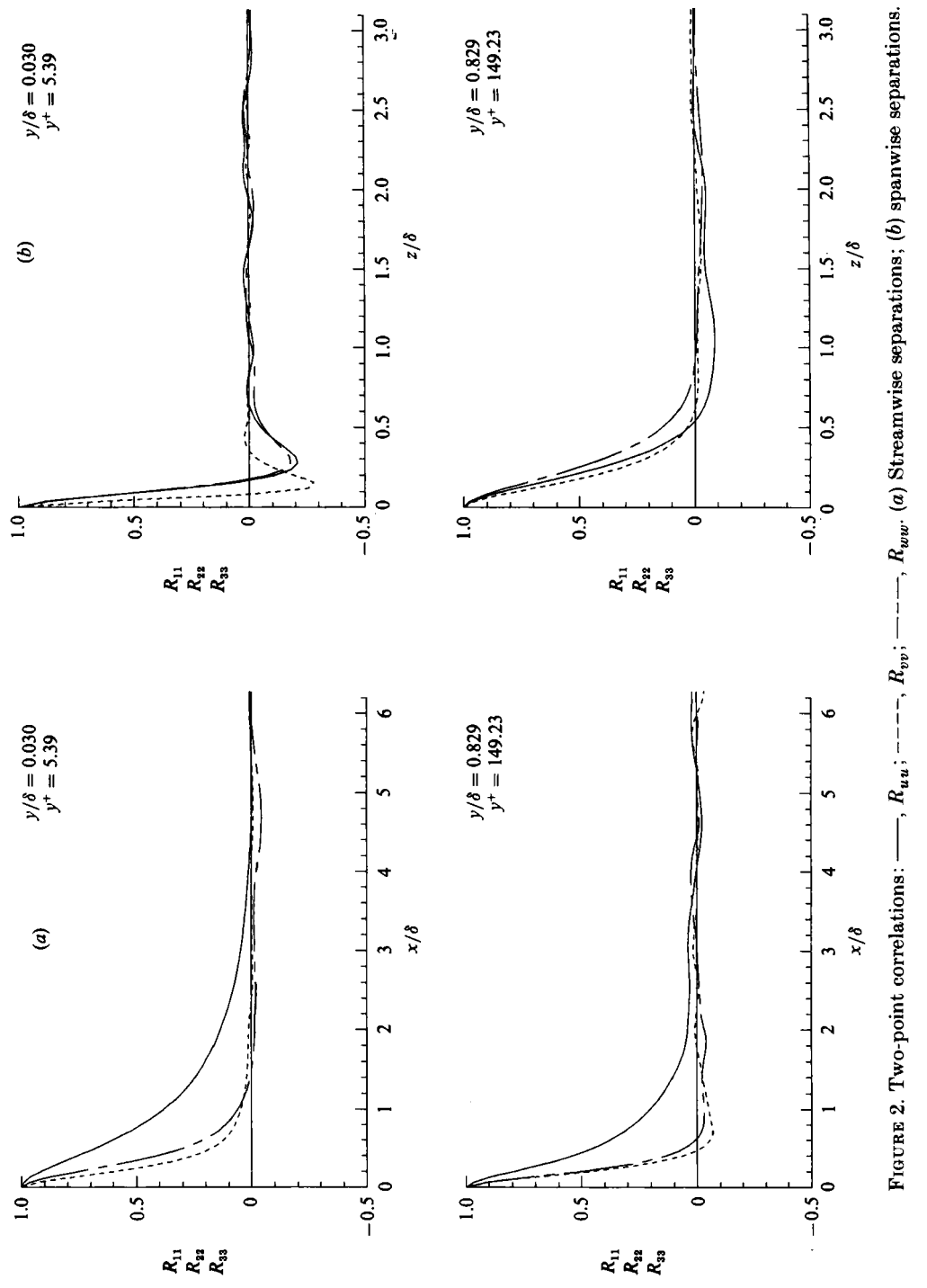

FIGURE 2. Two-point correlations: ——, R_{uu}; – – –, R_{vv}; — – —, R_{ww}. (*a*) Streamwise separations; (*b*) spanwise separations.

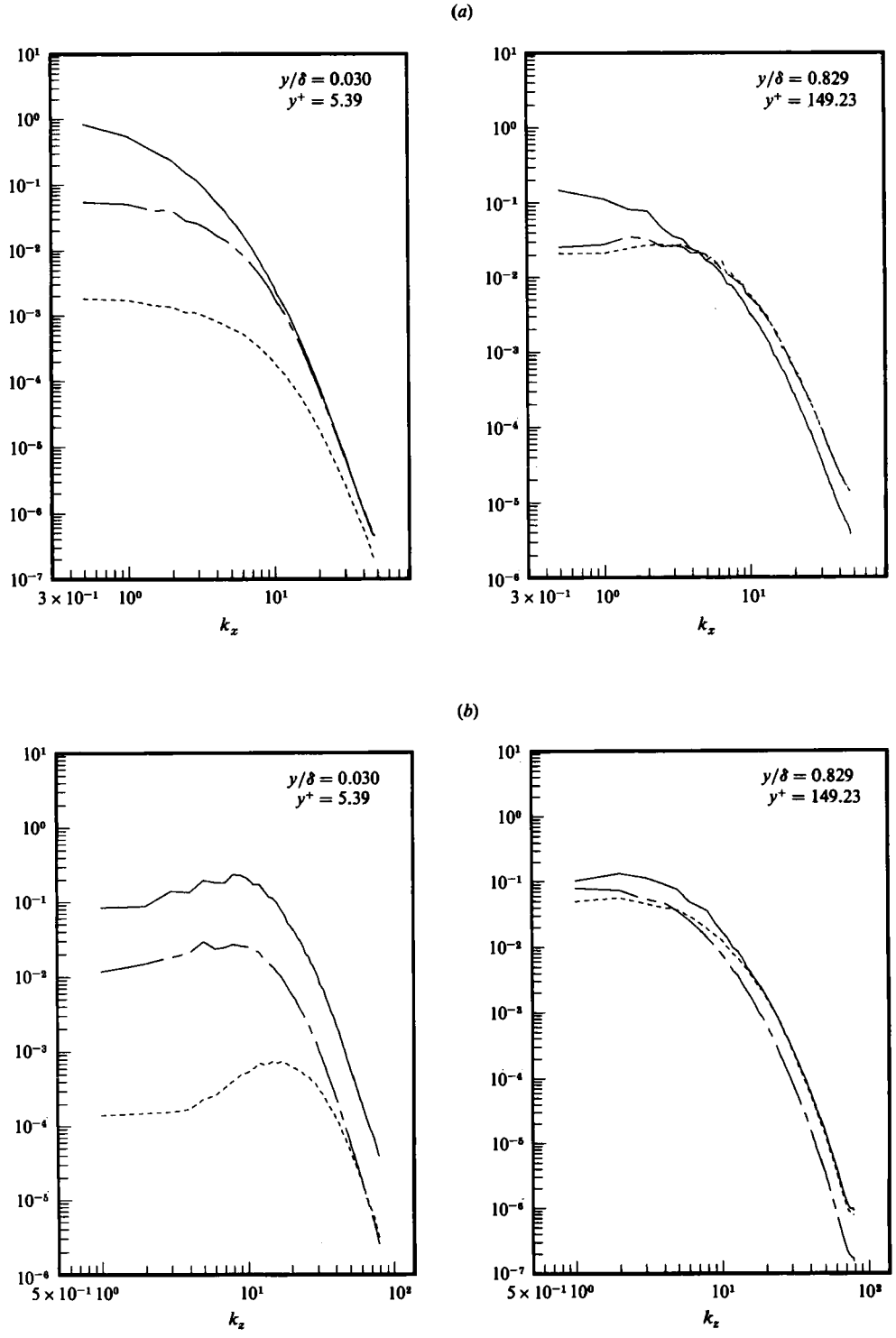

FIGURE 3. One-dimensional energy spectra: ——, E_{uu}; – – – –, E_{vv}; — — —, E_{ww}. (*a*) Streamwise; (*b*) spanwise.

wavenumbers is several decades lower than the energy density corresponding to low wavenumbers, and there is no evidence of energy pile-up at high wavenumbers.

It should be noted, however, that the drop-off of the computed spectra of high wavenumbers is not sufficient evidence that the computed results are unaffected by the small-scale motions neglected in the computations. It is not clear what significant dynamical roles, if any, these small scales would play if included in the computations. Numerical experiments with much finer resolutions than those used here would presumably clarify this issue. Such computations are very difficult and time consuming to carry out with the present computers. However, comparison of the present results with those obtained using a coarser mesh ($128 \times 129 \times 128$ in x, y, z) did not reveal any differences in the statistical correlations considered in this paper. This was also the case when we compared the present results with those obtained by Moser & Moin (1984) in which they used $128 \times 65 \times 128$ grid points in studying a turbulent flow in a curved channel at a comparable Reynolds number.

3. Numerical procedures

The governing equations for an incompressible flow can be written in the following form

$$\frac{\partial u_i}{\partial t} = -\frac{\partial p}{\partial x_i} + H_i + \frac{1}{Re}\nabla^2 u_i, \tag{1}$$

$$\frac{\partial u_i}{\partial x_i} = 0. \tag{2}$$

Here, all variables are non-dimensionalized by the channel half-width δ, and the wall shear velocity u_τ; H_i includes the convective terms and the mean pressure gradient; and Re denotes the Reynolds number defined as $Re = u_\tau \delta/\nu$.

Equations (1) and (2) can be reduced to yield a fourth-order equation for v, and a second-order equation for the normal component of vorticity as follows:

$$\frac{\partial}{\partial t}\nabla^2 v = h_v + \frac{1}{Re}\nabla^4 v, \tag{3}$$

$$\frac{\partial}{\partial t} g = h_g + \frac{1}{Re}\nabla^2 g, \tag{4}$$

$$f + \frac{\partial v}{\partial y} = 0, \tag{5}$$

where

$$f = \frac{\partial u}{\partial x} + \frac{\partial w}{\partial z}, \quad g = \frac{\partial u}{\partial z} - \frac{\partial w}{\partial x},$$

$$h_v = -\frac{\partial}{\partial y}\left(\frac{\partial H_1}{\partial x} + \frac{\partial H_3}{\partial z}\right) + \left(\frac{\partial^2}{\partial x^2} + \frac{\partial^2}{\partial z^2}\right) H_2,$$

$$h_g = \frac{\partial H_1}{\partial z} - \frac{\partial H_3}{\partial x}.$$

A spectral method – Fourier series in the streamwise and spanwise directions, and Chebychev polynomial expansion in the normal direction – is employed for the spatial derivatives. The time advancement is carried out by the same semi-implicit scheme

as in Moin & Kim (1982): Crank–Nicolson for the viscous terms and Adams–Bashforth for the nonlinear terms. Equation (4) then reduces to

$$\left.\begin{aligned}\left(1-\frac{\Delta t}{2Re}\nabla^2\right)g^{n+1} &= \frac{\Delta t}{2}(3h_g^n - h_g^{n-1}) + \left(1+\frac{\Delta t}{2Re}\nabla^2\right)g^n,\\ g(\pm 1) &= 0.\end{aligned}\right\} \tag{6}$$

Equation (6) is solved by the Chebychev–tau method (Lanczos 1956; Gottlieb & Orszag 1977) for each wavenumber after it is Fourier transformed in the streamwise and spanwise directions. It reduces to a tridiagonal system with one full row after decoupling the even and odd modes of the Chebychev coefficients.

The fourth-order equation (3) can be solved most efficiently by splitting it into two second-order equations as follows

$$\left.\begin{aligned}\left(1-\frac{\Delta t}{2Re}\nabla^2\right)\phi^{n+1} &= \frac{\Delta t}{2}(3h_v^n - h_v^{n-1}) + \left(1+\frac{\Delta t}{2Re}\nabla^2\right)\phi^n,\\ \nabla^2 v^{n+1} &= \phi^{n+1},\\ v^{n+1}(\pm 1) = \frac{\partial v^{n+1}}{\partial y}(\pm 1) &= 0.\end{aligned}\right\} \tag{7}$$

This coupled system is solved by the Chebychez–tau method, in which the four boundary conditions are satisfied as follows. Let

$$v^{n+1} = v_{\mathrm{p}}^{n+1} + c_1 v_1^{n+1} + c_2 v_2^{n+1}, \tag{8}$$

where the particular solution v_{p}^{n+1}, and the two homogeneous solutions v_1^{n+1} and v_2^{n+1} satisfy

$$\left.\begin{aligned}\left(1-\frac{\Delta t}{2Re}\nabla^2\right)\phi_{\mathrm{p}}^{n+1} &= \frac{\Delta t}{2}(3h_v^n - h_v^{n-1}) + \left(1+\frac{\Delta t}{2Re}\nabla^2\right)\phi^n,\\ \phi_{\mathrm{p}}^{n+1}(\pm 1) &= 0,\\ \nabla^2 v_{\mathrm{p}}^{n+1} &= \phi_{\mathrm{p}}^{n+1},\\ v_{\mathrm{p}}^{n+1}(\pm 1) &= 0,\end{aligned}\right\} \tag{9}$$

$$\left.\begin{aligned}\left(1-\frac{\Delta t}{2Re}\nabla^2\right)\phi_1^{n+1} &= 0,\\ \phi_1^{n+1}(1) = 0, \quad \phi_1^{n+1}(-1) &= 1,\\ \nabla^2 v_1^{n+1} &= \phi_1^{n+1},\\ v_1^{n+1}(\pm 1) &= 0,\end{aligned}\right\} \tag{10}$$

$$\left.\begin{aligned}\left(1-\frac{\Delta t}{2Re}\nabla^2\right)\phi_2^{n+1} &= 0,\\ \phi_2^{n+1}(1) = 1, \quad \phi_2^{n+1}(-1) &= 0,\\ \nabla^2 v_2^{n+1} &= \phi_2^{n+1},\\ v_2^{n+1}(\pm 1) &= 0.\end{aligned}\right\} \tag{11}$$

Equations (9)–(11) are solved after they are Fourier transformed in the streamwise and spanwise directions – in fact, they are solved simultaneously by eliminating the

same banded matrix with three different right-hand sides. The constants c_1 and c_2 are then chosen such that

$$\frac{\partial v^{n+1}}{\partial y}(\pm 1) = 0.$$

We note that this approach is similar to the Chebychev–tau/Green function technique used by Orszag & Patera (1981), except that here a linear combination of three intermediate solutions rather than five is required.

Once the normal velocity and vorticity are computed, the streamwise velocity u, and the spanwise velocity w, are then obtained from (5) and the definitions of f and g. Computation of pressure is not required for time advancement; it is calculated only to obtain turbulence statistics involving pressure. There are two ways to compute the pressure: either from the normal momentum equation with the wall pressure values determined from the combination of streamwise and spanwise momentum equations (the governing equation for f), or from the equation for f with the pressure corresponding to the zero wavenumbers ($k_x = k_z = 0$) determined from the normal momentum equation. For the present numerical method, there is no difference between the two results, indicating that the pressure satisfies both the Neumann and the Dirichlet boundary conditions (Gottlieb & Orszag 1977; Moin & Kim 1980). This consistency requirement is not preserved by some spectral codes.

The nonlinear terms in (1) are computed in the rotational form (see Moin & Kim 1982) to preserve the conservation property of mass, energy, and circulation numerically. In addition, the number of collocation points is expanded by a factor of $\frac{3}{2}$ before transforming into the physical space to avoid the aliasing errors involved in computing the nonlinear terms pseudo-spectrally.

The computations were carried out on the CRAY-XMP computer at NASA Ames Research Center. Since the required memory (about 28×10^6 words for 7 words per each grid point) was much larger than the central core memory, an external memory device was used during the computations. To reduce overhead due to I/O process, the database was arranged in the form of drawers so that it can be accessed from two different passes (transferring (x, z)- and (x, y)-planes to the core memory respectively). Data transfer between the core memory and the external device(s) was performed using a double-buffer scheme. When the Solid-State-Device (SSD) of CRAY-XMP was used as the external memory, double buffering was not necessary since the I/O wait time for this case was negligible. However, when external hard-disk devices were used, the above data management scheme results in significant savings in I/O wait time. The CPU time required for the computations with $192 \times 129 \times 160$ grid points was about 40 s per time step. The computations were carried out for about 10 non-dimensional time units (tu_τ/δ) using approximately 250 CPU hours.

The accuracy of the numerical code was examined by computing the evolution of small-amplitude oblique waves in a channel. Both decaying (stable) and growing (unstable) waves were tested for $Re_c = 7500$, based on the centreline velocity and the channel half-width. These initial conditions were obtained from numerical solutions of the Orr–Sommerfeld equations (Leonard & Wray 1982). With 65 Chebychev polynomials, both decay and growth rates were predicted to within $10^{-4}\%$ of the value predicted by the linear theory when the initial energy either decreased or increased by a factor of 10%.

4. Turbulence statistics

The initial velocity field used in the present work was obtained from the large-eddy simulation of Moin & Kim (1982). A velocity field from this ($64 \times 63 \times 128$)-calculation is interpolated onto the present collocation points by spectral interpolation and then integrated forward in time until the flow reaches a statistically steady state. The steady state is identified by a linear profile of total shear stress, $-\overline{u'v'} + (1/Re)\,\partial\overline{u}/\partial y$, and by quasi-periodic total kinetic energy. Once the velocity field reaches the statistically steady state, the equations are integrated further in time to obtain a running time average of the various statistical correlations. The statistical sample was further increased by averaging over horizontal planes (homogeneous directions). In this paper an overbar indicates an average over x, z and t, and a prime indicates perturbation from this average.

4.1. *Mean properties*

The profile of the mean velocity non-dimensionalized by the wall-shear velocity is shown in figure 4. The collapse of the mean-velocity profiles corresponding to the upper and lower half of the channel indicates the adequacy of the sample taken here for the average. Also shown in the figure is the mean-velocity profile from the experimental result of Eckelmann (1974) at $Re_\tau = 142 (Re_c = 2800)$. The dashed line represents the law of the wall and the log law. Within the sublayer, $y^+ < 5$, both the experimental and the computational results follow the linear law of the wall. In the logarithmic region, however, there exists a noticeable discrepancy between the two results. Note that 5.5 is used for the additive constant in the log law in contrast to 5.0, the value used in Moin & Kim (1982). The higher constant is a low-Reynolds-number effect ($Re_\tau = 180$ for the present work compared with 640 in Moin & Kim). However, the difference between the Reynolds number of the present work and that of Eckelmann is not large enough to cause the difference shown in the figure. In fact, the mean-velocity profile of Eckelmann (1974) for a slightly higher Reynolds number ($Re_\tau = 208$) collapses with his experimental data shown here (see figure 3 of Eckelmann 1974). The mean-velocity profile obtained earlier from the same facility at $Re_\tau = 187$, and reported by Wallace, Eckelmann & Brodkey (1972), agrees well with the present results (figure 1 of Wallace *et al.*). It is not clear why these results reported by Eckelmann (1974) and by Wallace *et al.* (1972) are significantly different from each other. Since the profile reported by Wallace *et al.* (1972) agrees well with the present results, we rescaled the mean-velocity profile reported by Eckelmann (1974) such that the two experimental results agree with each other at $y^+ = 100$. This amounts to increasing the u_τ of Eckelmann (1974) by 6 % (i.e. $u_{\tau c}/u_{\tau m} = 1.06$), where the subscripts c and m denote the corrected and measured values. This result is shown in figure 5 and shows an excellent agreement with the computed results.

Other mean properties such as the skin-friction coefficient, bulk mean velocity, displacement and momentum thicknesses are also computed from the computed mean-velocity profile. These computed values are compared with the experimental correlations proposed by Dean (1978). The bulk mean velocity, defined as

$$U_m = \frac{1}{2}\int_{-1}^{1} \overline{u}\,\mathrm{d}\left(\frac{y}{\delta}\right),$$

normalized by the wall-shear velocity, is 15.63, which gives the Reynolds number based on the bulk mean velocity and the full channel width, $Re_m \approx 5600$. The skin friction coefficient, $C_f = \tau_w/\frac{1}{2}\rho U_m^2$ is 8.18×10^{-3}, which is in good agreement with

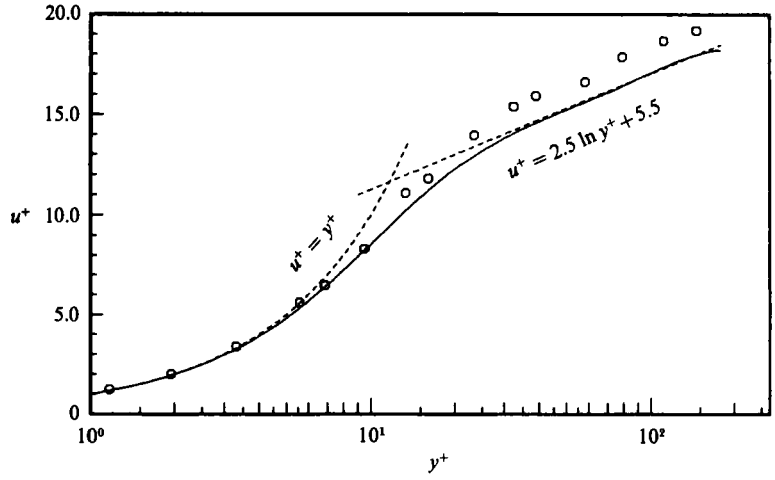

FIGURE 4. Mean-velocity profiles: ——, upper wall; — — —, lower wall (masked by solid line); ○, data from Eckelmann (1974); – – – –, law of the wall.

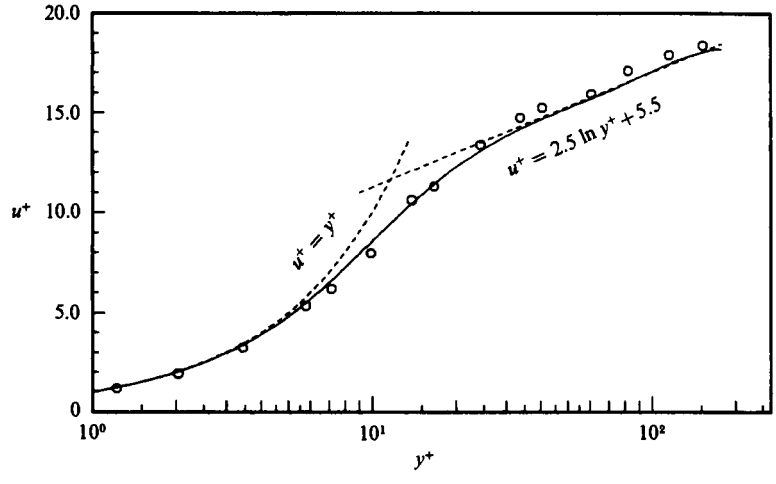

FIGURE 5. Mean-velocity profiles: ——, upper wall; — — —, lower wall (masked by solid line); ○, 'corrected' data of Eckelmann (1974); – – – –, law of the wall.

Dean's suggested correlation of $C_f = 0.073\, Re_{\mathrm{m}}^{-0.25} = 8.44 \times 10^{-3}$. The ratio of the mean centreline velocity to the mean bulk velocity, $U_{\mathrm{c}}/U_{\mathrm{m}}$, is 1.16, an excellent agreement with Dean's correlation of $U_{\mathrm{c}}/U_{\mathrm{m}} = 1.28\, Re_{\mathrm{m}}^{-0.0116} = 1.16$. Other computed mean properties are shown in table 1. Comparisons of these computed bulk flow variables with the experimental data compiled by Dean show excellent agreement.

4.2. *Turbulence intensities*

Turbulence intensities normalized by the wall-shear velocity are shown in figure 6, and they are compared with those at Reynolds numbers $Re_\tau = 194$ from Kreplin & Eckelmann (1979, hereinafter denoted KE). The symmetry of the profiles about the channel centreline again indicates the adequacy of the sample taken for the average. Although the general shape of the profiles is in good agreement, there exists some discrepancy between the two results. The computed results for all three components

$$Re_\tau = \frac{u_\tau \delta}{\nu} \approx 180 \qquad C_f = \frac{\tau_w}{\frac{1}{2}\rho U_m^2} = 8.18 \times 10^{-3}$$

$$Re_c = \frac{U_c \delta}{\nu} \approx 3300 \qquad C_{f_0} = \frac{\tau_w}{\frac{1}{2}\rho U_c^2} = 6.04 \times 10^{-3}$$

$$Re_m = \frac{U_m 2\delta}{\nu} \approx 5600 \qquad \frac{\delta^*}{\delta} = 0.141$$

$$\frac{U_m}{u_\tau} = 15.63 \qquad \frac{\theta}{\delta} = 0.087$$

$$\frac{U_c}{u_\tau} = 18.20 \qquad H = \frac{\delta^*}{\theta} = 1.62$$

$$\frac{U_c}{U_m} = 1.16 \qquad G = \frac{U_c}{u_\tau}\left(\frac{H-1}{H}\right) = 6.97$$

TABLE 1. Mean flow variables

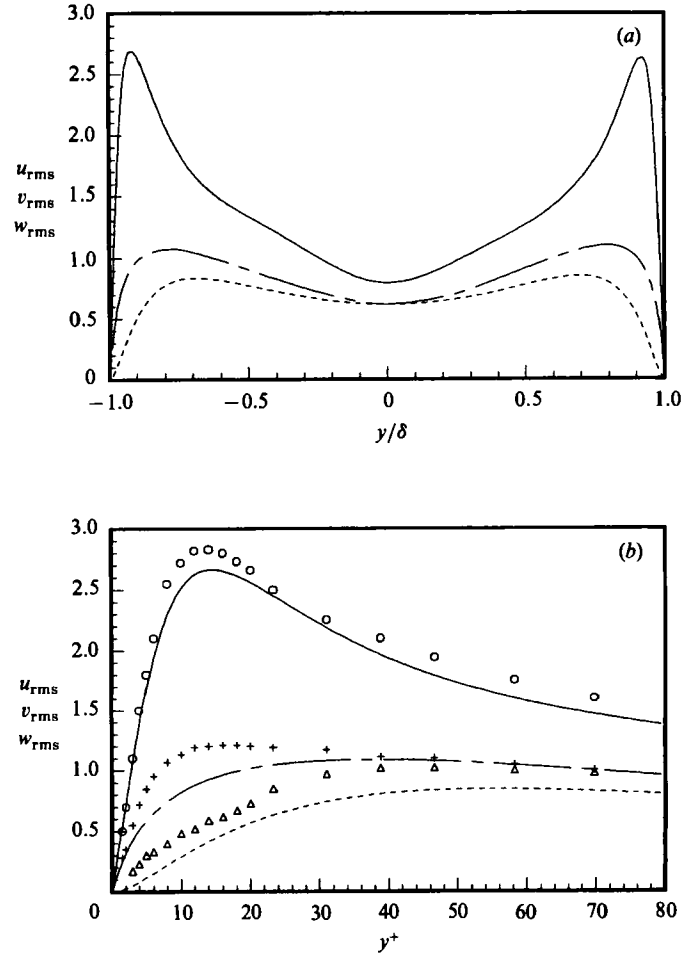

FIGURE 6. Root-mean-square velocity fluctuations normalized by the wall shear velocity: ——, u_{rms}; – – –, v_{rms}; — — —, w_{rms}. (*a*) In global coordinates; (*b*) in wall coordinates. Symbols represent the data from Kreplin & Eckelmann (1979): ○, u_{rms}; △, v_{rms}; +, w_{rms}.

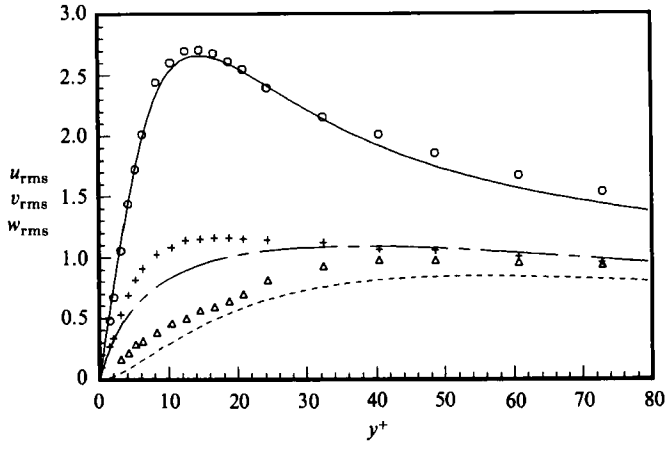

FIGURE 7. Same as in figure 6(*b*), but with the experimental data renormalized by the 'corrected' wall shear velocity.

are lower than the measured values. Since the level of the normal component of intensity is the lowest, it has the largest fractional difference. In accordance with the rescaling of the mean-velocity profile discussed above, the turbulence intensities are renormalized by u_{τ_c} and are shown in figure 7. With the new scaling the overall agreement is improved, but the computed results are still lower than the measured values, except the streamwise fluctuations. However, Perry, Lim & Henbest (1985) point out that most of the existing data in the wall region measured by the standard hot-wire techniques – especially for the normal component – may contain significant error caused by cross-contamination, where an X-wire signal sensitive to v is also sensitive to the velocity component normal to the plane of the wires. This error would result in higher measured values for the normal and spanwise components. Further careful experimental verification is required to clarify this issue. The location of the maximum streamwise fluctuation is at $y^+ \approx 12$ for both cases, which also corresponds to the location of the maximum production, i.e. $-\overline{u'v'}(\partial\overline{u}/\partial y)$.

In figure 8, turbulence intensities are normalized by the local mean velocity $\overline{u}$. The limiting values of these quantities should approach the wall values of streamwise, normal, and spanwise vorticity fluctuations normalized by the mean velocity gradient at the wall. For comparison, the experimental data of KE and Hanratty *et al.* (1977, hereinafter denoted HCH) are shown in the same figure. The experimental points are from their curve fit through the data; the data points of HCH are in fact from a fit through scattered experimental data by several investigators. It can be seen that there are discrepancies among the reported results in the near-wall region. For example, $u_{\rm rms}/\overline{u}$ of the present result and HCH approach asymptotic values of 0.37 and 0.3, respectively, whereas the result of KE shows a maximum at $y^+ \approx 5$ and then approaches 0.25 at the wall.† Note that this asymptotic value corresponds to the normalized wall value of the spanwise vorticity fluctuation. A similar discrepancy is noticeable for $w_{\rm rms}/\overline{u}$ (streamwise vorticity at the wall). The present result shows that this quantity reaches the maximum value of 0.2 at the wall, while that of KE

† J. H. Haritonidis & A. V. Johansson (1985, private communication) performed new measurements in the oil channel used by Eckelmann and his co-workers, and they reported that the new measurements indicated $u_{\rm rms}/\overline{u}$ approached about 0.4 without a decrease near the wall, which is in good agreement with the present results. They attributed the error to the heat-conduction problem in the proximity of the wall.

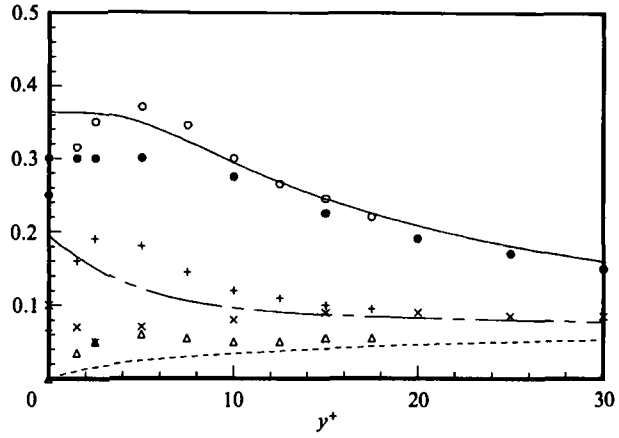

FIGURE 8. Turbulence intensities near the wall normalized by the local mean velocity: ——, $u_{\rm rms}/\overline{u}$; – – – –, $v_{\rm rms}/\overline{u}$; — — —, $w_{\rm rms}/\overline{u}$. From Kreplin & Eckelmann (1979): ○, $u_{\rm rms}/\overline{u}$; △, $v_{\rm rms}/\overline{u}$; +, $w_{\rm rms}/\overline{u}$. From Hanratty, Chorn & Hatziavramidis (1977): ●, $u_{\rm rms}/\overline{u}$; ×, $w_{\rm rms}/\overline{u}$.

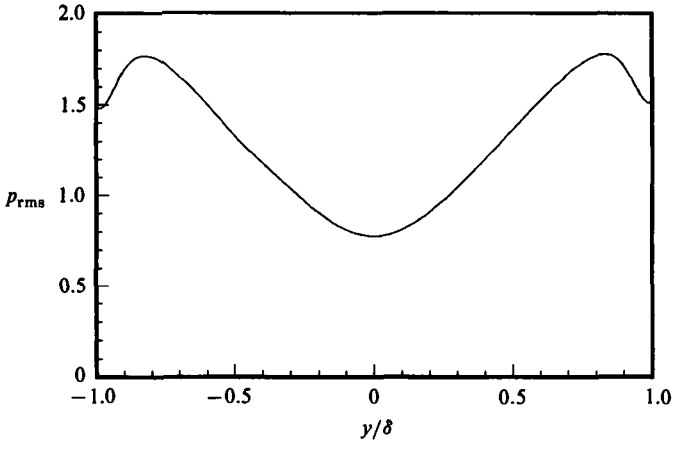

FIGURE 9. Root-mean-square pressure fluctuations normalized by the wall shear velocity, $p_{\rm rms}/\rho u_\tau^2$.

decreases near the wall with the wall value of 0.065, and the result of HCH shows a dip near $y^+ = 2.5$ before it increases to 0.1. These different wall behaviours result in significantly different wall values of the vorticity fluctuations, except the normal component, which is zero at the wall. Different experimental results reported in KE (table 1 of KE) indicate that the spanwise vorticity at the wall varies from 0.205 to 0.3 while the streamwise vorticity varies from 0.065 to 0.115.

Figure 9 shows the profile of root-mean-square (r.m.s.) pressure normalized by the wall shear velocity, $p_{\rm rms}/\rho u_\tau^2$. It has a maximum value of 1.75 at $y^+ \approx 30$ and approaches 1.5 at the wall. This r.m.s. wall pressure is somewhat lower than the experimental results compiled by Willmarth (1975), which show that the r.m.s. wall pressure in turbulent boundary layers varies between 2 and 3. Note, however, that the Reynolds number of the present calculation is much lower than the Reynolds-number range in the experimental measurements. Willmarth (1975) shows a definite decreasing trend of the r.m.s. wall-pressure fluctuations with Reynolds number (see

figure 7 of Willmarth).† In a previous simulation at a higher Reynolds number ($Re_c = 13800$, Moin & Kim 1982), the r.m.s. wall pressure was about 2.0. Willmarth also considered the effect of the size of transducers on the measured r.m.s. wall pressure, and showed that it increases significantly with smaller probes. Since the grid resolution of the present calculation is much finer than that of Moin & Kim, the reduction in the r.m.s. wall pressure appears to be due to the low Reynolds number.

4.3. *Reynolds shear stress*

The Reynolds shear stress and the correlation coefficient are shown in figures 10 and 11, respectively. Also shown in figure 10(*a*) is the total shear stress, $-\overline{u'v'} + (1/Re)\,\partial\overline{u}/\partial y$. In the fully developed channel flow considered here, this profile is a straight line when the flow reaches an equilibrium state. The computed result clearly indicates that this is the case. The computed shear stress is compared with the experimental results in figure 10(*b*). The results shown in the figures correspond to three slightly different Reynolds numbers: $Re_\tau = 180$ for the present computation and $Re_\tau = 142$ and 208 for Eckelmann's (1970) data.‡ The behaviour of the Reynolds shear stress in the immediate vicinity of the wall for a fully-developed channel flow can be deduced from the following equation (Tennekes & Lumley 1972):

$$-\frac{\overline{u'v'}}{u_\tau^2} + \frac{\mathrm{d}u^+}{\mathrm{d}y^+} = 1 - \frac{y^+}{\delta^+}.$$

Non-dimensionalized in this way, the Reynolds-number dependence is absorbed into δ^+. Thus for small y^+/δ^+, the Reynolds shear stress for different Reynolds numbers should collapse into one curve. For example, for the three Reynolds numbers considered here, the difference in $(-\overline{u'v'})/u_\tau^2$ should be less than 0.022 at $y^+ < 10$, but the difference between the measurements and computations at $y^+ = 10$ is about 0.1. Although the two experimental results collapse into each other, the computed result is lower. However, considering the expected y^3 behaviour of the Reynolds shear stress in the immediate vicinity of the wall (§4.4), the experimental results seem to be too high in the wall region. In figure 10(*c*), the measured Reynolds shear stresses are rescaled by $(u_{\tau_m}/u_{\tau_c})^2$ as before. The discrepancy in the wall region persists, although the overall agreement between the present results and the experimental results corresponding to $Re_\tau = 208$ is satisfactory for $y^+ > 10$. The profile of the correlation coefficient (figure 11) is in good agreement with that of Sabot & Comte-Bellot (1976), although the Reynolds number of their flow was much higher ($Re_c = 68000$ and 135000 based on the centreline velocity and the pipe diameter). This suggests the correlation coefficient is less dependent on the Reynolds number than are the Reynolds stresses. It is interesting to note that the present result shows a local peak at $y^+ \approx 12$, which is also the location of the maximum production and the maximum streamwise velocity fluctuation. This peak, although rather weak, was also observed in the large-eddy simulation of Moin & Kim (1982) as well as in the direct simulation of a curved channel flow (Moser & Moin 1984) where it was attributed to certain organized motions in the wall region. The limiting wall values of the correlation coefficient and other stresses are given in table 2.

† P. Bradshaw (1985, private communication) shows that if one assumes that the power spectra of wall pressure has $1/k$-dependence, then the r.m.s. wall pressure would have a logarithmic dependence on the Reynolds number: i.e. $p_{\mathrm{rms}} = c_1 + c_2 \ln(u_\tau \delta/\nu)$.

‡ The data points are obtained from figure 10(*a*) of Hanjalic & Launder (1976).

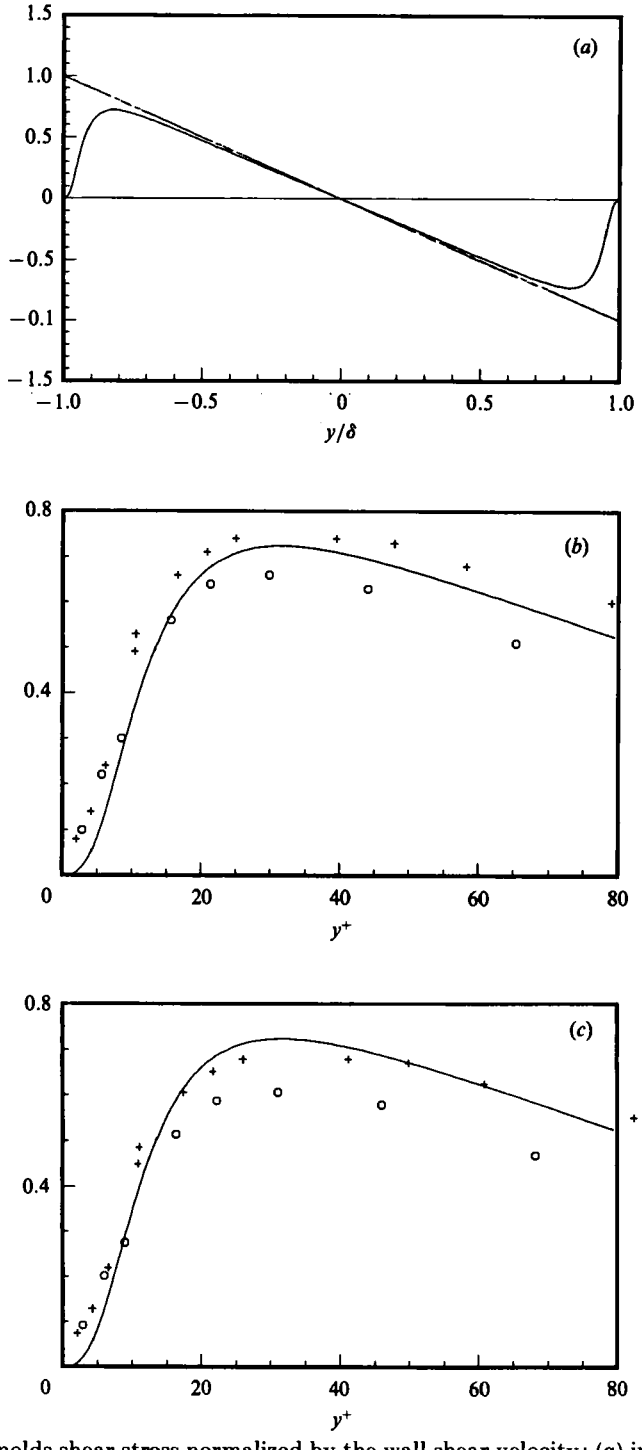

FIGURE 10. Reynolds shear stress normalized by the wall shear velocity: (*a*) in global coordinates, ——, $-\overline{u'v'}$; — — —, $-\overline{u'v'}+(1/Re)\partial\overline{u}/\partial y$; – – – –, total shear stress for fully developed channel; (*b*) in wall coordinates, ——, $-\overline{u'v'}$; ○, data from Eckelmann (1974) for $Re_\tau = 142$; +, data from Eckelmann for $Re_\tau = 208$; (*c*) same as (*b*) except the data are renormalized by 'corrected' u_τ.

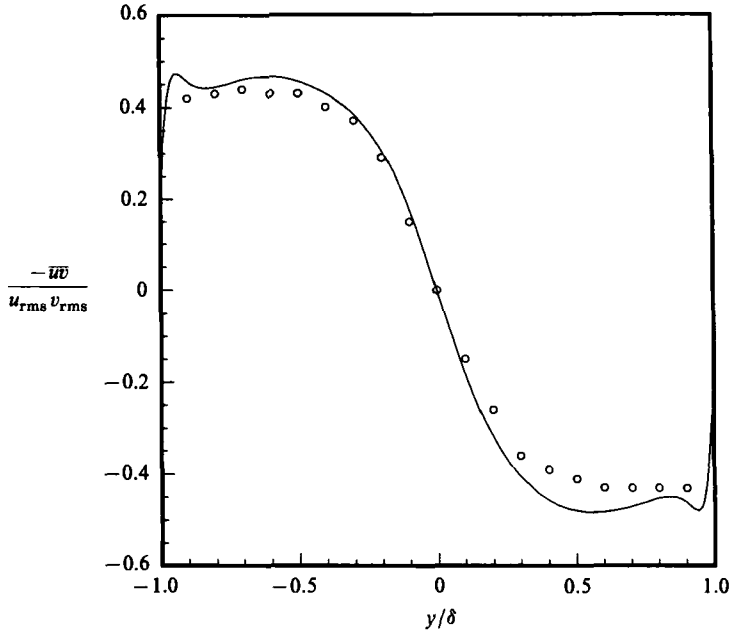

FIGURE 11. Correlation coefficient of u' and v': ——, computation; ○, data from Sabot & Comte-Bellot (1976).

y^+	$u^+_{\rm rms}/y^+$	$v^+_{\rm rms}/y^{+2}\times 10^3$	$w^+_{\rm rms}/y^+$	$-\overline{u^+v^+}/y^{+3}\times 10^4$	$-\overline{uv}/u_{\rm rms}\, v_{\rm rms}$
0.05381	0.3637	8.616	0.1940	7.212	0.2301
0.2152	0.3634	8.425	0.1903	7.284	0.2379
0.4841	0.3629	8.119	0.1845	7.399	0.2512
0.8603	0.3623	7.714	0.1768	7.542	0.2699
1.344	0.3615	7.233	0.1677	7.681	0.2938
1.934	0.3601	6.700	0.1575	7.765	0.3218
2.630	0.3574	6.138	0.1466	7.729	0.3524
3.433	0.3522	5.570	0.1355	7.516	0.3831
4.341	0.3435	5.015	0.1246	7.092	0.4117
5.354	0.3305	4.489	0.1141	6.468	0.4360
6.472	0.3131	4.000	0.1043	5.697	0.4549
7.693	0.2921	3.553	0.09543	4.855	0.4679
9.018	0.2685	3.151	0.08739	4.019	0.4751
10.44	0.2439	2.790	0.08014	3.248	0.4773

TABLE 2. Near-wall behaviour of Reynolds stresses

4.4. *Near-wall behaviour of Reynolds stresses*

The limiting wall behaviour of the Reynolds stresses is shown in figure 12. From the figure, it is apparent that

$$\left.\begin{aligned} u_{\rm rms} &= a_1 y + a_2 y^2 + \ldots, \\ v_{\rm rms} &= b_1 y^2 + b_2 y^3 + \ldots, \\ u_{\rm rms} &= c_1 y + c_2 y^2 + \ldots, \\ \overline{u'v'} &= d_1 y^3 + d_2 y^4 + \ldots. \end{aligned}\right\} \tag{12}$$

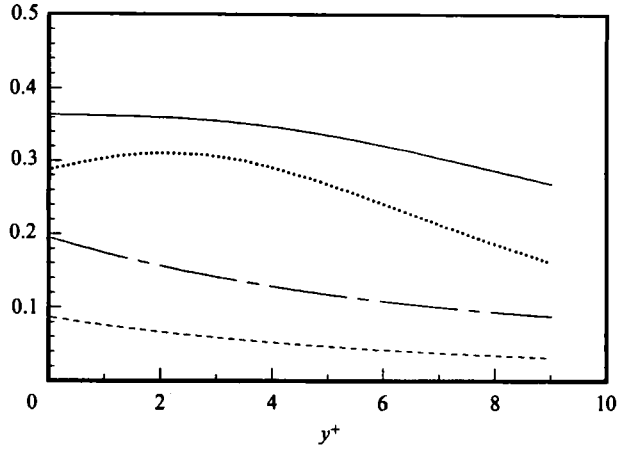

FIGURE 12. Near-wall behaviour of Reynolds stresses: ——, $u^+_{\rm rms}/y^+$; — — —, $w^+_{\rm rms}/y^+$; – – – –, $10v^+_{\rm rms}/y^{+2}$; · · · · · ·, $400(-\overline{u'v'})/y^{+3}$.

The y-behaviour of the tangential stresses and the y^2 behaviour of the normal stress are expected from consideration of the no-slip boundary condition and the continuity equation. However, the limiting behaviour of the shear stress has been a subject of some disagreement. Hinze (1975) describes the controversy over y^3 *vs.* y^4. Ohji (1967) claimed it should be y^4; Chapman & Kuhn (1985) showed that y^4 behaviour of Ohji's analysis was due to an erroneous assumption. The present numerical result seems to support the y^3 behaviour. The same behaviour was also observed in a recent direct simulation of a turbulent boundary layer by Spalart (1985).

Finnicum & Hanratty (1985) estimated the limiting behaviour of v, and reported $v_{\rm rms} \approx 0.005y^{+2}$. The present result indicates $v_{\rm rms} \approx 0.009y^{+2}$ (see table 2). We note, however, that if one uses $0.2u_\tau^2/\nu$ as the wall value of r.m.s. streamwise vorticity fluctuation (the wall value of the present simulation) instead of $0.11u_\tau^2/\nu$ as used in their analysis, one obtains $v_{\rm rms} \approx 0.0083y^{+2}$, which is in good agreement with the present result. It appears that their analysis and measurements, including the estimation of the Taylor microscales from the two-point correlation measurements, are consistent with the present results. The discrepancy is due to the different wall values of streamwise vorticity used in their analysis. A comparison of the present results of the near-wall behaviour of v with the data presented in figure 7 of Finnicum & Hanratty is shown in figure 13. The present results fall below all the experimental data, but they are above the results of Nikolaides and Hanratty, whose results are obtained from their near-wall model. Note that $v_{\rm rms}/y^2$ should approach a constant at the wall, but the experimental data do not show this behaviour. In fact some of the data, especially those of Eckelmann and of Ueda, indicate $v_{\rm rms} \sim y$, which is not compatible with the continuity equation at the wall. Finnicum & Hanratty concluded from this figure that reliable measurements cannot be made with an X-probe for $y^+ < 10$.

4.5. *Vorticity*

Vorticity fluctuations normalized by the mean shear at the wall ($\omega_i \nu/u_\tau^2$) are shown in figure 14(*a*). Away from the wall, the three components of the fluctuating vorticity are identical. In figure 14(*b*), the vorticity fluctuations in the wall region are plotted *vs.* y^+. In addition streamwise vorticity fluctuations measured by Kastrinakis

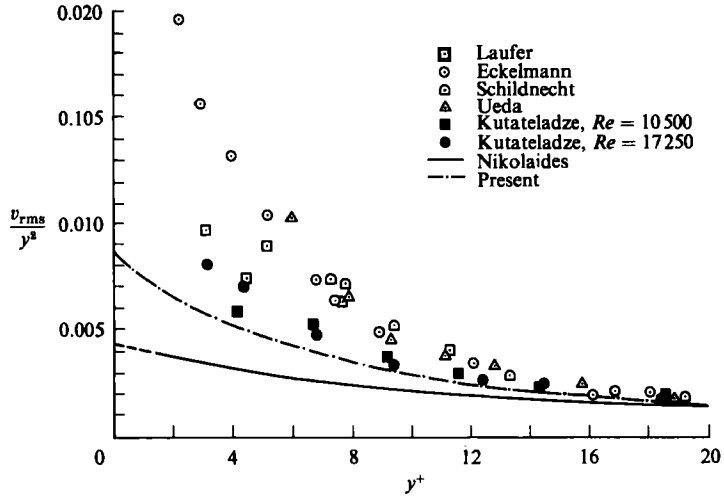

FIGURE 13. Comparison of the near-wall behaviour of the normal velocity fluctuation with experimental data from Finnicum & Hanratty (1985).

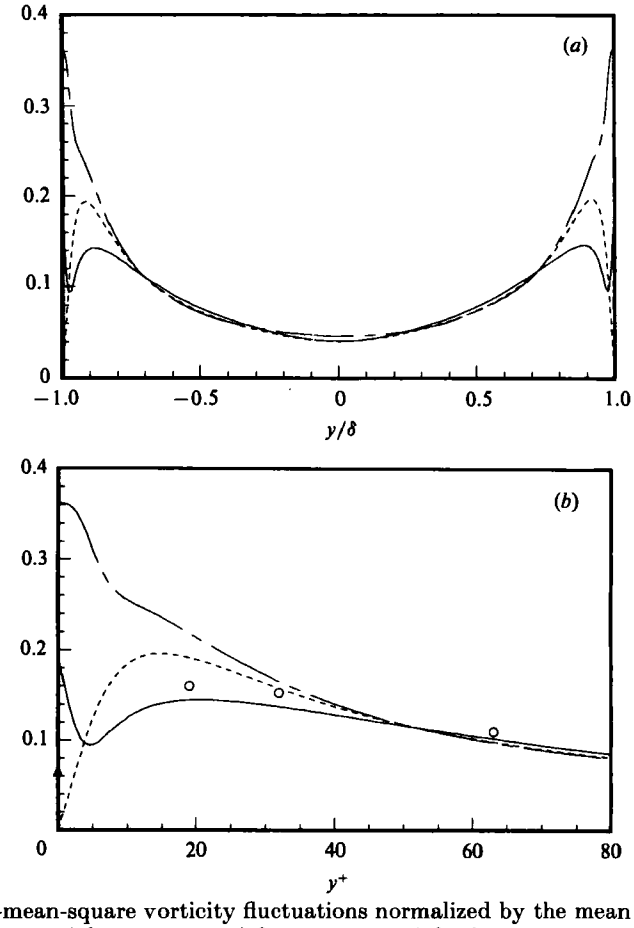

FIGURE 14. Root-mean-square vorticity fluctuations normalized by the mean shear. (*a*) In global coordinates: ——, $\omega_x \nu/u_\tau^2$; – – – –, $\omega_y \nu/u_\tau^2$; — · —, $\omega_z \nu/u_\tau^2$; (*b*) in wall cordinates: ○, ω_x from Kastrinakis & Eckelmann (1983), △, ω_x at the wall from Kreplin & Eckelmann (1979).

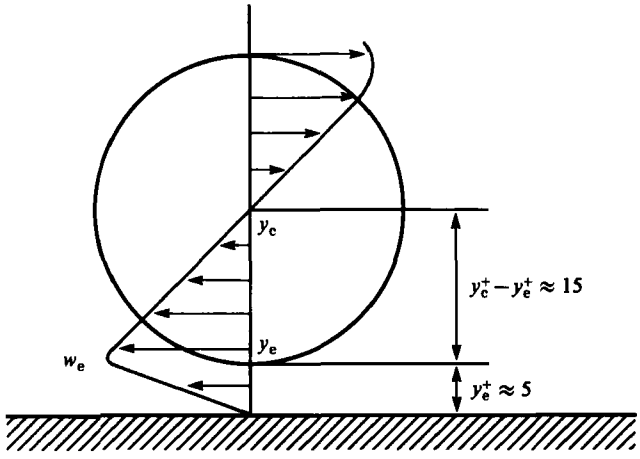

FIGURE 15. A streamwise vortex model responsible for high streamwise vorticity at the wall.

& Eckelmann (1983) and the streamwise vorticity fluctuation at the wall reported by Kreplin & Eckelmann (1979) are also plotted for comparison. The computed streamwise vorticity agrees well with the existing experimental results for y^+ greater than about 20, where the computed profile shows a local maximum. Unfortunately, no data exist between $y^+ \approx 20$ and the wall, and the measured wall values vary significantly, as mentioned earlier (between 0.065 and 0.115). The computed result shows a local minimum at about $y^+ = 5$ before it attains the maximum value at the wall. The same behaviour was observed in the numerical results of Moin & Kim (1982), Moser & Moin (1984), and Spalart (1985). Moser & Moin attributed this behaviour – the presence of a local maximum and minimum in the streamwise vorticity – to streamwise vortices in the wall region. They reasoned that the location of the local maximum corresponds to the average location of the centre of the streamwise vortices and the local minimum is caused by the streamwise vorticity with opposite sign created at the wall because of the no-slip boundary condition. In a single realization (and assuming the existence of vortical structures near the wall), the streamwise vorticity must become zero somewhere between the centre of the vortex and the wall, but on the average its r.m.s. value would have a local minimum at the average location of the edge of the vortex, since its size and location vary in time and space. It can be estimated then from figure 14 (*b*) that the centre of the streamwise vortex is located on the average at $y^+ \approx 20$ with radius $r^+ \approx 15$ (see figure 15) and strength about $0.13 u_\tau^2/\nu$. This estimate of the size of the streamwise vortex from the profile of r.m.s. streamwise vorticity near the wall is in good agreement with the experimental results of Smith & Schwartz (1983). From this flow module, one can estimate the magnitude of streamwise vorticity at the wall caused by the presence of the streamwise vortex. If we assume that the velocity distribution inside the vortex is similar to that of a Rankine vortex (see figure 15), then for the spanwise velocity fluctuations, we have

$$\left|\frac{\partial w}{\partial y}\Big|_w\right| \approx \left|\frac{w_e}{y_e}\right| = \left|\frac{w_e}{y_c - y_e}\right| \frac{y_c - y_e}{y_e} = 3\left|\frac{w_e}{y_c - y_e}\right|$$

$$\approx 3\left|\frac{\partial w}{\partial y}\Big|_c\right|,$$

where the subscripts c, e and w denote the centre of the vortex, the edge of the vortex and the wall, respectively. Since

$$\left|\omega_x\right|_c = \left|\frac{\partial w}{\partial y}\right|_c - \frac{\partial v}{\partial z}\Big|_c = 2\left|\frac{\partial w}{\partial y}\right|_c$$

for the Rankine vortex,

$$\left|\frac{\partial w}{\partial y}\right|_w \approx \tfrac{3}{2}\left|\omega_x\right|_c = \tfrac{3}{2}0.13\frac{u_\tau^2}{\nu}$$

$$\approx 0.19\frac{u_\tau^2}{\nu}.$$

This is in good agreement with the computed results shown in figure 14(*b*). Admittedly, the model in figure 15 is crude, but this flow module does provide a vorticity field consistent with the behaviour of the computed streamwise vorticity near the wall. Note that no assumption is made regarding the streamwise extent of the streamwise vortices.

4.6. *Quadrant analysis*

The quadrant analysis of the Reynolds shear stress provides detailed information on the contribution to the total turbulence production from various events occurring in the flows (Willmarth & Lu 1972; Wallace *et al.* 1972). The analysis divides the Reynolds shear stress into four categories according to the signs of u' and v'. The first quadrant, $u' > 0$ and $v' > 0$, contains outward motion of high-speed fluid; the second quadrant, $u' < 0$ and $v' > 0$, contains the motion associated with ejections of low-speed fluid away from the wall; the third quadrant, $u' < 0$ and $v' < 0$, contains inward motion of low-speed fluid; and the fourth quadrant, $u' > 0$ and $v' < 0$, contains an inrush of high-speed fluid, sometimes referred to as the sweep event. Thus the second- and fourth-quadrant events contribute to the negative Reynolds shear stress (positive production), and the first- and third-quadrant events contribute to the positive Reynolds shear stress (negative production). This analysis also has been used to detect the organized structures associated with the bursting event in channel flow (Kim & Moin 1985). The contribution to the Reynolds shear stress from each quadrant as a function of y-location is shown in figure 16 along with the experimental data of Willmarth & Lu (1972), Brodkey, Wallace & Eckelmann (1974), and Barlow & Johnston (1985). Wallace *et al.* (1972) also reported similar data, which are significantly different from those of Brodkey *et al.*, but Brodkey *et al.* later attributed the difference to anomalies in the data-reduction process. Both the experimental results and the present results display the dominance of the ejection event (second quadrant, $u' < 0$ and $v' > 0$) away from the wall with the sweep event (fourth quadrant, $u' > 0$ and $v' < 0$) dominating in the wall region; at $y^+ \approx 12$, they are about the same. Although the general characteristics of the present results – such as the crossing point and the dominance of sweep and ejection events in different regions – are in agreement with the experimental data, there exists a significant quantitative difference, especially in the near-wall region. However, there are significant differences, even among different experimental results, as shown in figure 16. In particular, the results by Brodkey *et al.* indicate that large negative contributions originate from the first and third quadrants which are observed neither in the present results nor in those of Barlow & Johnston (1985). The present results seem to agree better with those of Barlow & Johnston, although they did not make measurements close to the wall.

Fractional contributions from the four quadrants to the total Reynolds shear stress

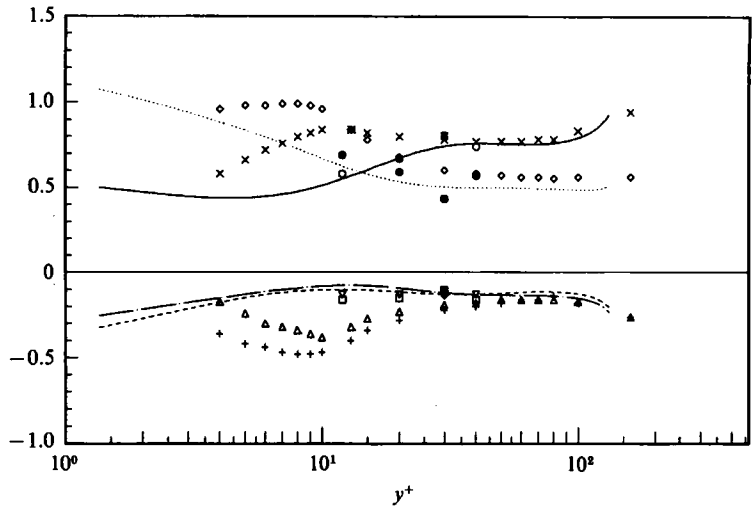

FIGURE 16. Reynolds shear stress from each quadrant normalized by the local mean Reynolds shear stress: ----, first; ——, second; — — —, third; · · · · · ·, fourth quadrant. Symbols represent the experimental data: +, first; ×, second; △, third; ◇, fourth quadrant from Brodkey *et al.* (1974); □, first; ○, second; ▽, third; ●, fourth quadrant from Barlow & Johnston (1985); ⊠, first; ⧓, second; ⊕, third; ⊕, fourth quadrant from Willmarth & Lu (1972).

at three y-locations are shown in figure 17. The present results are in good agreement with the experimental data of Alfredsson & Johansson (1984), who measured only at $y^+ \approx 50$. At $y^+ \approx 50$ (figure 17*c*), where the ejection events dominate, about 80% of the total shear stress is due to the ejections, and the intense $u'v'$ events, say $-u'v' > 3u_{\rm rms}v_{\rm rms}$, are essentially from the second quadrant. This situation reverses in the wall region, as indicated in figure 17(*a*), where the fractional contribution at $y^+ \approx 8$ is shown. Here most of the large values of $u'v'$ are due to the events in the fourth quadrant. At $y^+ \approx 12$, the approximate location where the contributions from the ejection and sweep events are about the same, figure 17(*b*) indicates that even their fractional distributions are identical with each other.

4.7. *Higher-order statistics*

The computed skewness and flatness factors of u_i' and p' are shown in figure 18(*a*, *b*). Unlike the lower-order statistics presented in the previous sections, these figures show that the adequacy of the sample size used to compute the higher-order statistics is only marginal, as indicated by the small asymmetry and oscillations in the profiles. The skewness of w', which should be zero because of the reflection symmetry of the solutions of the Navier–Stokes equations, also indicates the marginal sample size.

The skewnes and flatness factors of all the quantities shown here are significantly different from those values for a Gaussian distribution (0 and 3, respectively). It is interesting to note that the flatness factor of pressure is significantly higher than that of the velocity fluctuations in the central region of the channel, indicating that the pressure fluctuation is more intermittent throughout the channel, except near the wall. As the wall is approached, the flatness factor of pressure fluctuations becomes about 5, while that of v' becomes about 22 (out of the range shown in figure 18*b*), indicating the highly intermittent character of the normal velocity near the wall.

In figures 19 and 20, the skewness and flatness factors for each component are compared with measurements from KE and Barlow & Johnston (1985). Note that

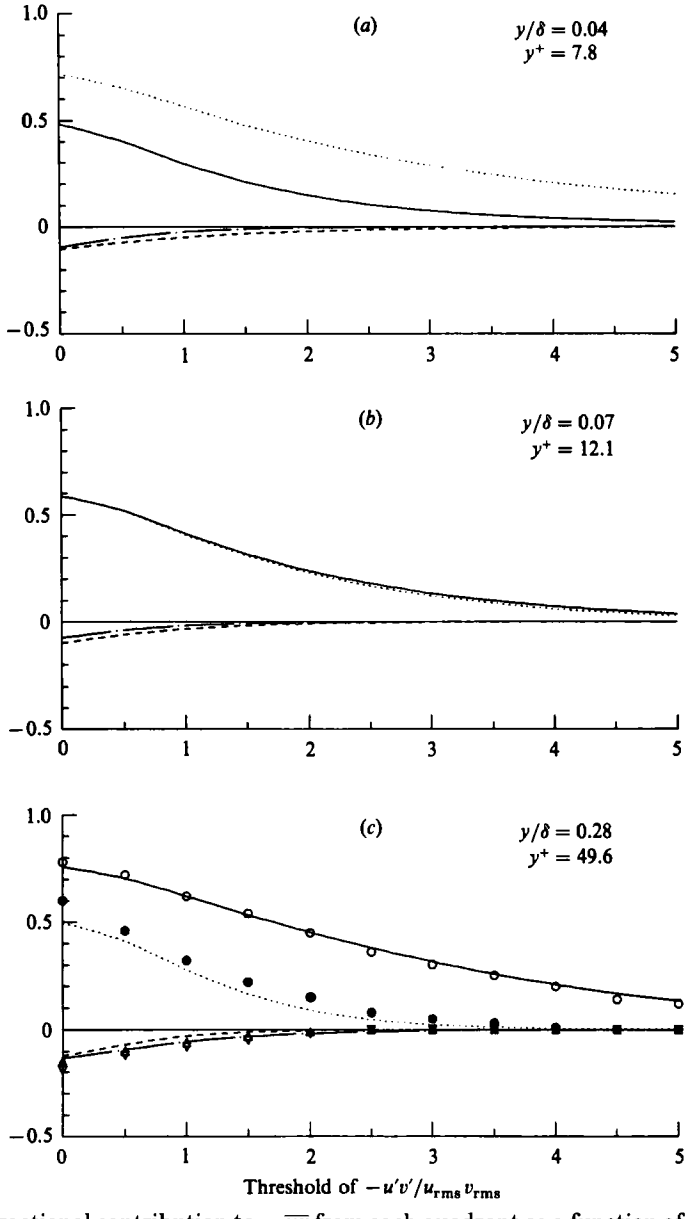

FIGURE 17. Fractional contribution to $-\overline{uv}$ from each quadrant as a function of threshhold; ----, first; ——, second; — — —, third; · · · · · ·, fourth quadrants: (*a*) $y^+ \approx 8$; (*b*) 12; (*c*) 50. Symbols represent the interpolated data at $y^+ = 50$ from figure 3 of Alfredsson & Johansson (1984): △, first; ○, second; ▽, third; ●, fourth quadrant.

the experimental results of Barlow & Johnston correspond to a turbulent boundary layer whereas those of KE and the present results correspond to a turbulent channel. Agreements among the computed and measured values are satisfactory for u' and w', but there exists a significant discrepancy for v', especially for the flatness factor in the vicinity of the wall. While the computed results show that the flatness factor approaches about 22, both measurements show that it decreases as the wall is approached. The laser-Doppler velocimeter (LDV) measurements by Barlow &

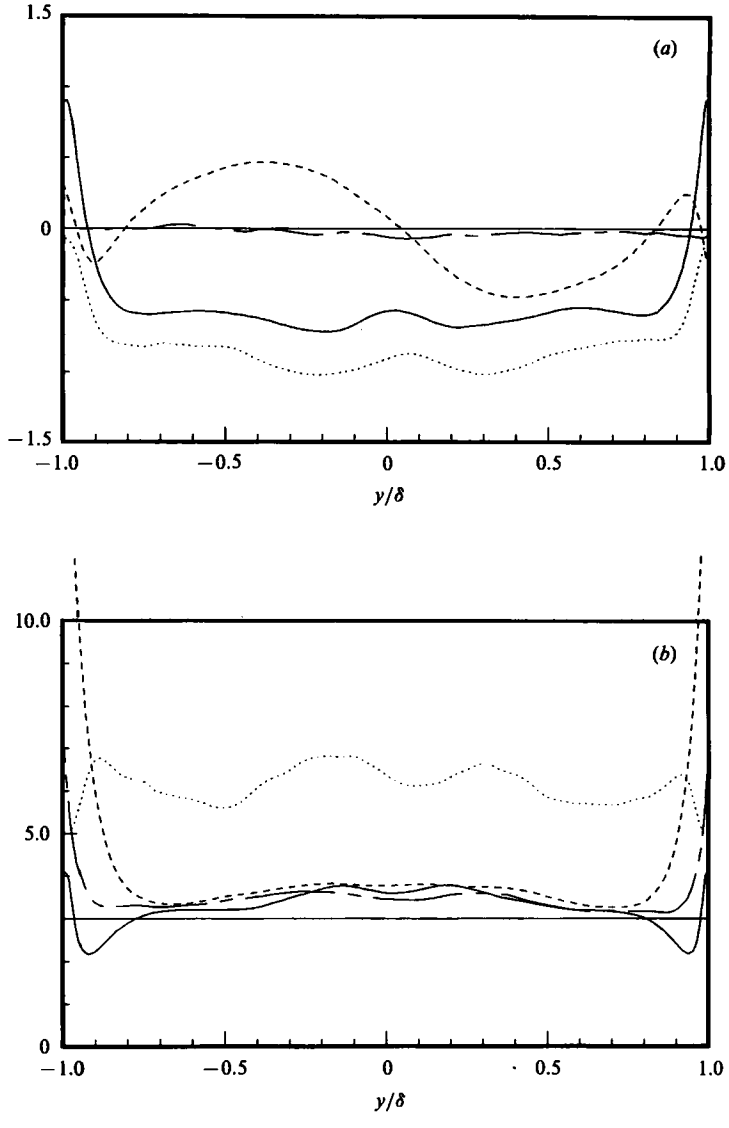

FIGURE 18. Skewness and flatness factors in global coordinates. (*a*) Skewness, ——, $S(u')$; – – –, $S(v')$; — — —, $S(w')$; · · · · · ·, $S(p')$. (*b*) Flatness, ——, $F(u')$; – – –, $F(v')$; — — —, $F(w')$; · · · · · ·, $F(p')$.

Johnston are suspect near the wall, say $y^+ < 10$, since the signal-to-noise ratio was too low (R. S. Barlow 1985, private communication). The data of KE obtained by a hot-film anemometer are also likely to be affected by the wall proximity. The computed skewness of v' does not agree with measurements of KE, but it is in good agreement with that of Barlow & Johnston, including the crossover point at $y^+ \approx 30$. For $y^+ < 10$, the agreement between computed and experimental data is again not good. Agreement between the present results and those from Moser & Moin (1984) is very good, with the exception that the overall magnitudes are either decreased (convex side) or increased (concave side) as a result of the curvature effect.

The behaviour of the skewness of v' near the wall is somewhat unexpected, whereas that of u' is as expected from the quadrant analysis in §4.6; that is, the most violent

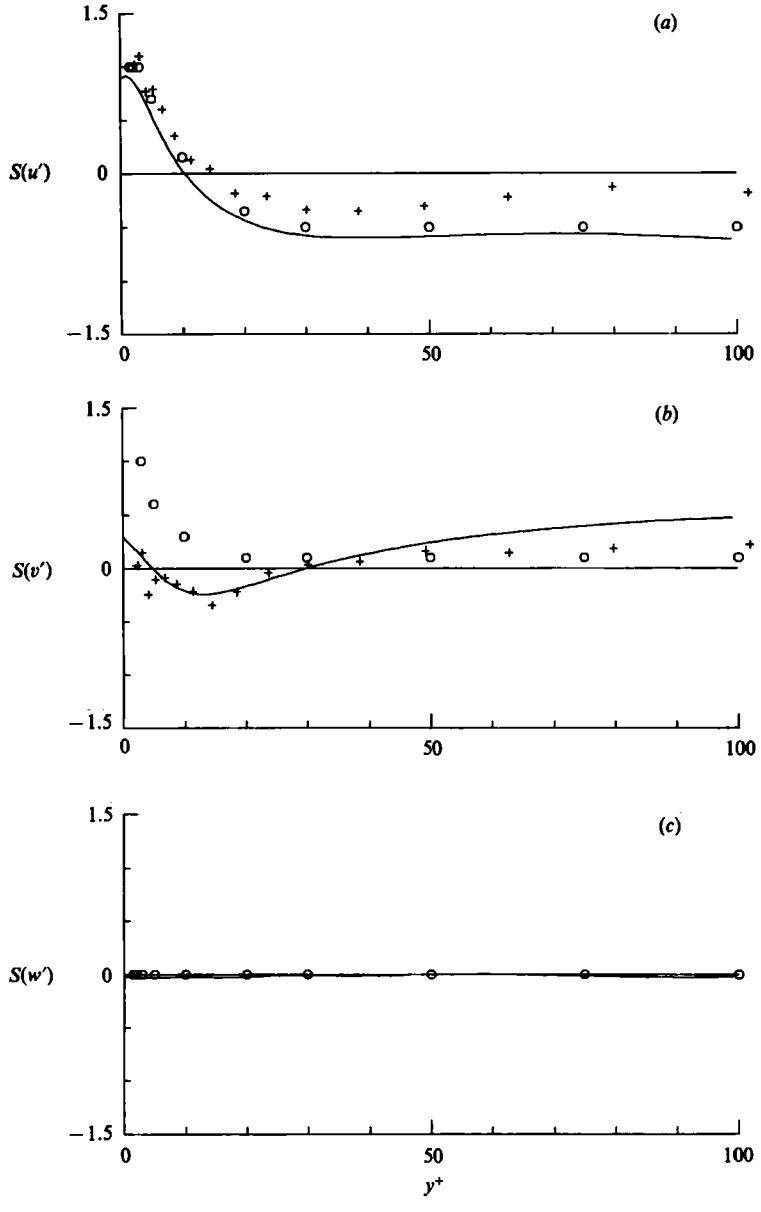

FIGURE 19. Skewness factors in wall coordinates: ——, computed; ○, Kreplin & Eckelmann (1979); +, Barlow & Johnston (1985): (*a*) $S(u')$; (*b*) $S(v')$; (*c*) $S(w')$.

Reynolds shear-stress-producing events are from the second quadrant ($u' < 0$ and $v' > 0$) for $y^+ > 12$, while they are from the fourth quadrant ($u' > 0$ and $v' < 0$) for $y^+ < 12$. According to the profile of skewness of v', there exist strong positive v' motions for $y^+ > 30$, strong negative v' motions for $6 < y^+ < 30$, and then strong positive v' motions for $y^+ < 6$. Note that the term 'strong' is used here relative to the local r.m.s. value. This suggests that in the region $12 < y^+ < 30$, where the skewness of both u' and v' is negative, the large excursions of negative v' (responsible for the negative skewness) are not correlated with the large excursions of negative u' (responsible for the negative skewness of u'); otherwise, we would have large

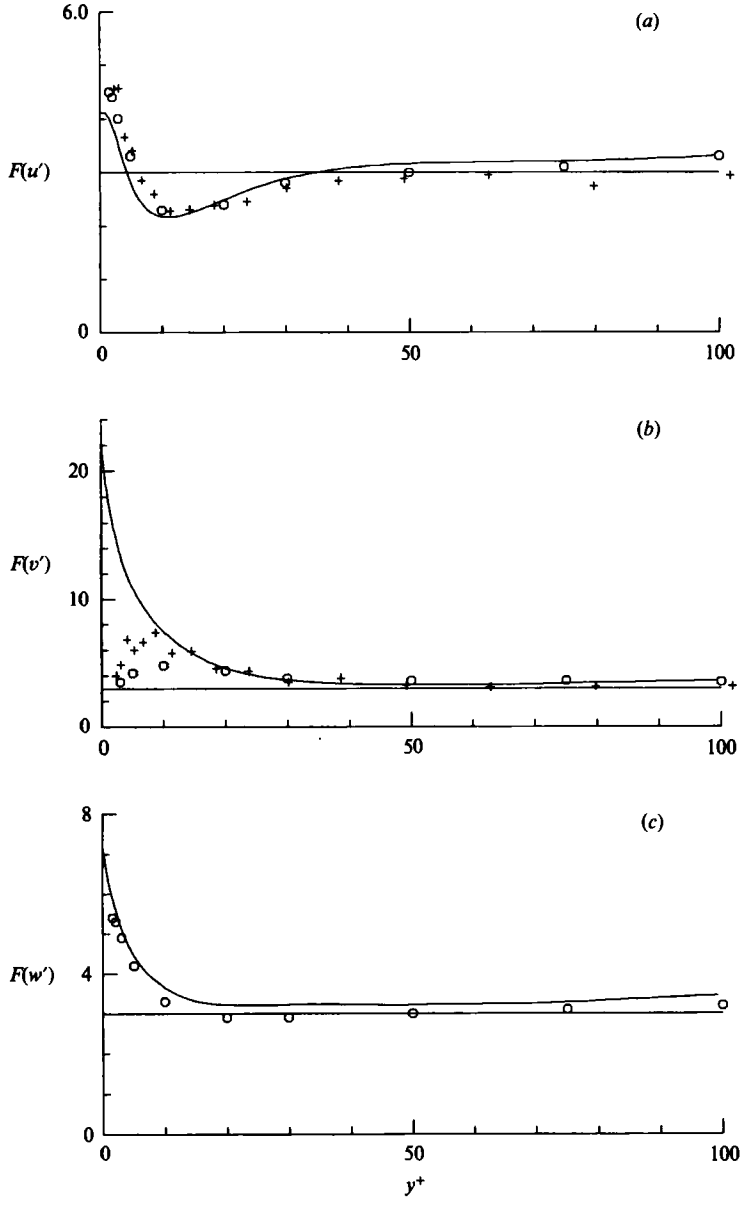

FIGURE 20. Flatness factors in wall coordinates: ——, computed; ○, Kreplin & Eckelmann (1979); +, Barlow & Johnston (1985): (*a*) $F(u')$; (*b*) $F(v')$; (*c*) $F(w')$. A flatness of 3 corresponding to a Gaussian distribution is also shown for a reference.

contributions of positive Reynolds shear stress from the third quadrant. Figure 21 (*c*) shows a plot of $u'v'$ distribution at $y^+ \approx 20$ obtained from instantaneous values of u' and v' at all grid points in this plane, where the skewness of both u' and v' is negative and large values of $u'v'$ are from the second quadrant. The skewnesses of u' and v' for the data shown in the figure (only a small fraction of the total sample used in computing the statistics is shown here) are -0.35 and -0.18, respectively. The dashed lines in the figure represent hyperbolas corresponding to $|u'v'| = 8 \times -\overline{u'v'}$; symbols outside the hyperbolas indicate $u'v'$ larger that eight times the mean

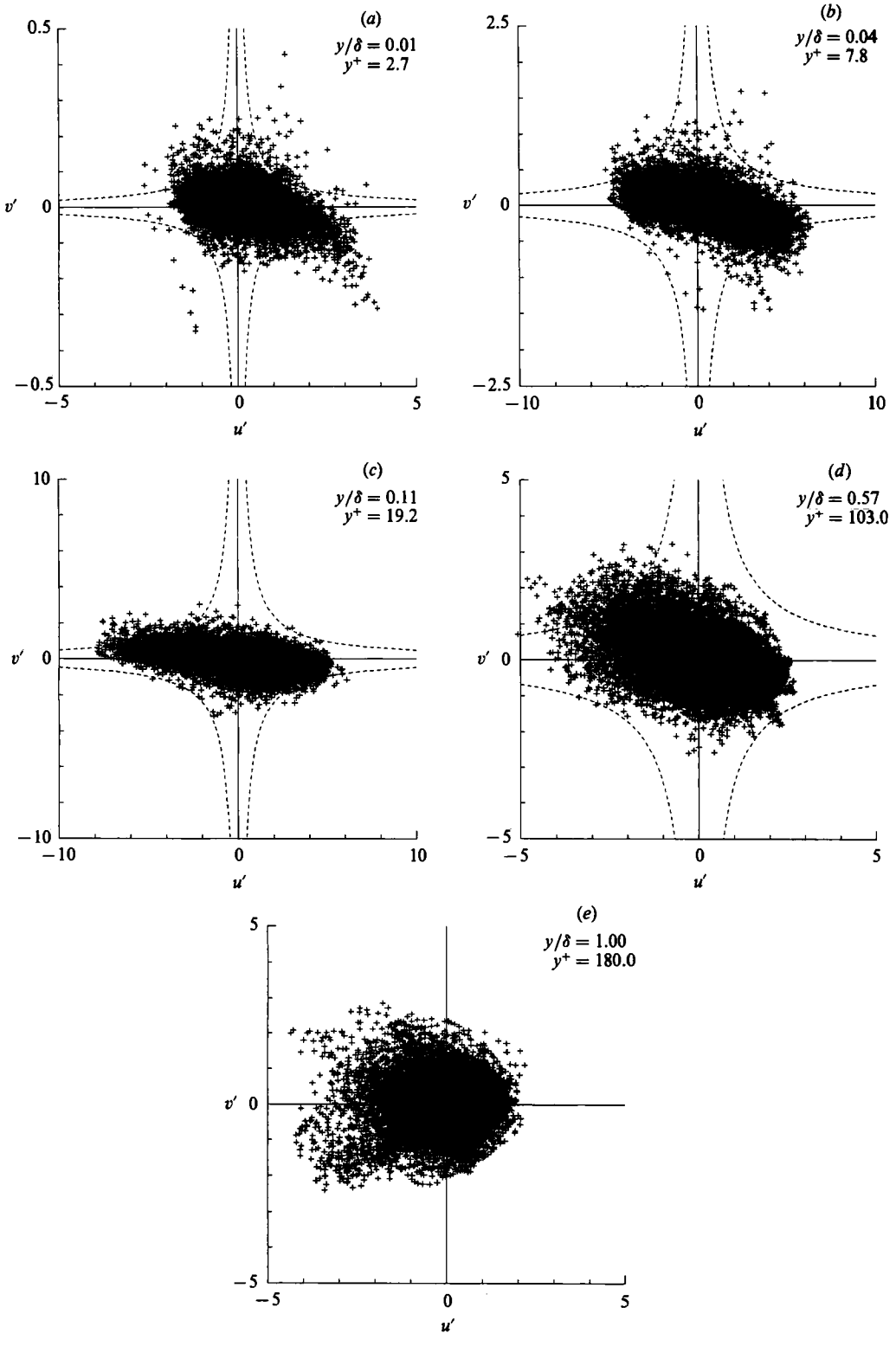

FIGURE 21. Distribution of (u', v'): (a) $y^+ \approx 3$; (b) 8; (c) 20; (d) 100; (e) 180. The dashed lines in the figures represent hyperbolas corresponding to $|u'v'| = 8 \times -\overline{u'v'}$.

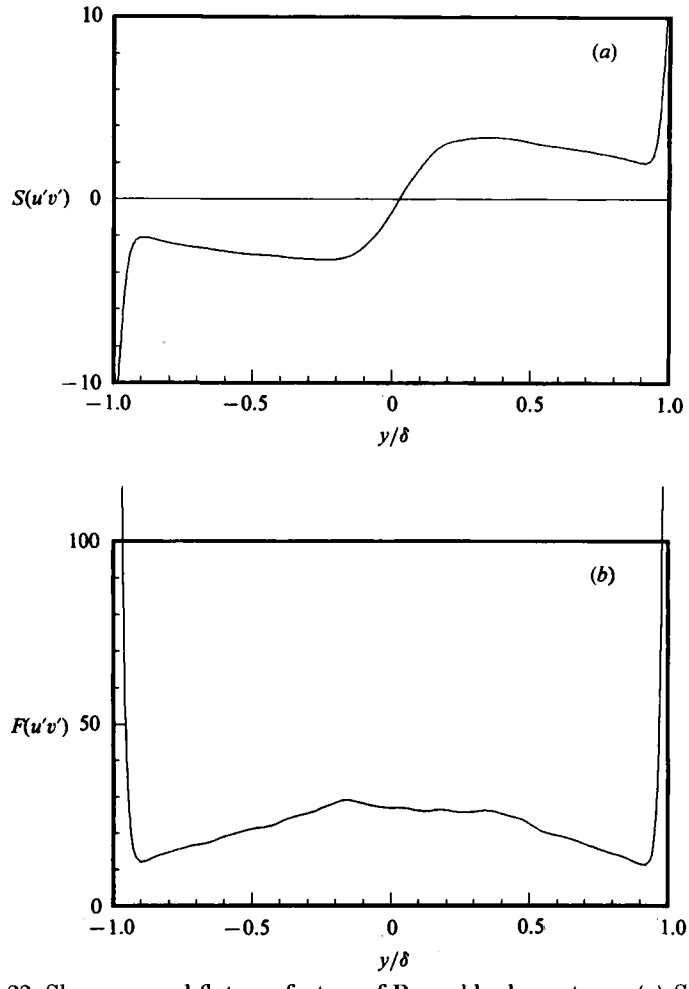

FIGURE 22. Skewness and flatness factors of Reynolds shear stress: (*a*) $S(u'v')$; (*b*) $F(u'v')$.

Reynolds shear stress. As indicated from the quadrant analysis, the large negative v' is not correlated with the large negative u'. It also shows that the events responsible for the large negative Reynolds shear stress are from large negative u' and positive v'. Figure 21 (*a*) shows a similar plot at $y^+ \approx 2.7$, where the skewness factors of u' and v' are both positive (0.9 and 0.24 respectively). Note that the ordinate is expanded by a factor of 10. Here the events associated with large positive u' are responsible for the negative Reynolds shear stress, while the events associated with large positive v' are not. Figure 21 (*b*) shows a similar plot at $y^+ \approx 8$, where the skewness of u' is positive and that of v' is negative. Here, the large positive u' responsible for the positive skewness is well correlated with the large negative v' responsible for the negative skewness of v', resulting in a large negative $u'v'$. Figure 21 (*d*, *e*) shows similar plots at $y^+ \approx 100$ and $y^+ \approx 180$. Note that at the centreline of the channel (figure 21 *e*), where the mean Reynolds shear stress is zero, there are many events associated with large $u'v'$, but they average to zero – the large negative $u'v'$ corresponds to the second quadrant (ejection) of the lower wall while the large positive $u'v'$ corresponds to the ejection events of the upper wall.

The skewness and flatnes factors of the Reynolds shear stress shown in figure 22

have higher values than those of turbulence intensities. The skewness is about -2 to -3 (or 2 or 3) with a slight increase in magnitude toward the centreline – except near the centreline of the channel where it should go through zero by the symmetry – and approaches about -10 (or 10) very close to the wall. The flatness factor is about 20, again with a slight increase toward the channel centreline and approaches about 200 very close to the wall, indicating the extremely intermittent nature of the Reynolds shear-stress-producing events near the surface. Gupta & Kaplan (1972) measured the high-order statistics of the Reynolds shear stress in turbulent boundary layers, and their measurements also indicate high skewness and flatness factors in the wall region; the highest values were obtained at the point nearest the wall (-6 and 104 for the skewness and flatness factors, respectively). However, these values – including the skewness and flatness factors for the velocity components near the wall – should be accepted with some reservation, since both the denomenator and the numerator of the skewness and flatness factors becomes zero as the wall is approached, and any inaccuracy in its measurement (or computation) could be excessively amplified.

5. Turbulence structures

The database of Moin & Kim (1982) has been used extensively in investigating the organized structures associated with well-bounded shear flows (Kim 1983, 1985; Moin 1984; Moin & Kim 1985). Although essentially all qualitative features of their results were in good agreement with experimental data, some quantitative structural information such as the streak spacing in the wall region was not consistent with experimental results because of the coarse mesh used in the computation. The present computation, with $\Delta z^+ \approx 7$, should have a sufficient grid resolution for the formation of the wall-layer streaks, observed experimentally to have a mean spacing of $\Delta z^+ \approx 100$. Contour plots of streamwise velocity in the wall region (not shown) in addition to the two-point autocorrelation of the streamwise velocity at points separated in the spanwise direction (figure 23), clearly indicate that the streaks are properly resolved in the present simulation. This correlation becomes negative and reaches a minimum at $\Delta z^+ \approx 50$. The separation at which this minimum occurs provides an estimate of the mean separation between the high- and low-speed fluid, and the mean spacing between the streaks should be roughly twice the distance. The presence of the minimum of R_{vv} at $\Delta z^+ \approx 25$ is consistent with the existence of streamwise vortical structures in the wall region. The separation of minimum R_{vv} corresponds to the mean diameter of the streamwise vortex. These results are consistent with the numerical results of Moser & Moin (1984), who observed the same behaviour in their direct simulation of a mildly curved channel flow. The presence of a minimum in the profile of R_{ww} at $\Delta z^+ \approx 50$ appears to indicate the presence of counter-rotating vortex pairs. However, as pointed out by Moser & Moin, since a minimum in R_{ww} does not occur for $y^+ > 30$, the minimum in R_{ww} at $y^+ \approx 10$ is more likely to be due to the impingement or splatting effect which can be caused by a single vortex. The mean streak spacing as a function of the distance from the wall can be evaluated by examining the two-point correlations at various y-locations. This result is shown in figure 24 together with the experimental results reported by Smith & Metzler (1983). In agreement with the experimental observations, the computed streak spacing increases with the distance from the wall.

In figure 25, examples of two visualization techniques are shown. In figure 25(*a*), hydrogen-bubble flow visualization is simulated by generating particles along a line

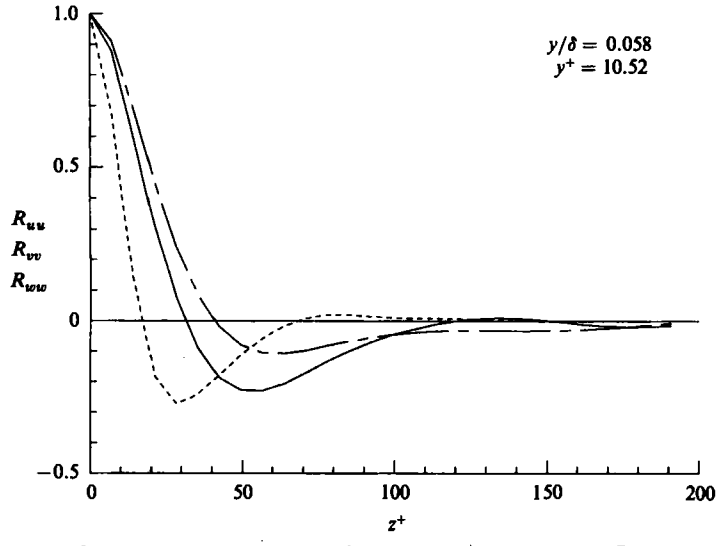

FIGURE 23. Spanwise two-point correlations at $y^+ \approx 10$: ——, $R_{uu}(z)$; – – – –, $R_{vv}(z)$; ——–, $R_{ww}(z)$.

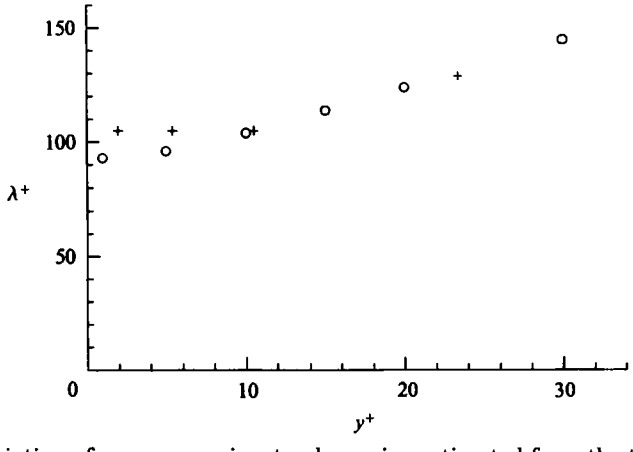

FIGURE 24. Variation of mean spanwise streak spacing estimated from the two-point correlations, $R_{uu}(z)$, and comparison with experimental data: +, present; ○, Smith & Metzler (1983).

parallel to the z-axis at $y^+ \approx 10$. The resulting pattern illustrates the formation of low- and high-speed streaks in the wall region. On the other hand, figure 25(*b*) is obtained by tracking particles initially distributed on a plane parallel to the wall at $y^+ \approx 10$. The initial sheet of particles is distorted by the instantaneous velocity field. Visualized in this way – this should be similar to the visualization of a smoke-filled boundary layer illuminated by a laser sheet parallel to the wall – flow patterns similar to the pocket flow module (Falco 1980) are visible. Figure 25(*a*, *b*) illustrates how different aspects of flow characteristics are emphasized by different visualization methods. The particles in figure 25(*c*) were generated along a line parallel to the y-axis. They illustrate the violent vortical motions associated with the bursting event in a way similar to that of the flow-visualization photographs obtained using a vertical hydrogen-bubble wire by Kim, Kline & Reynolds (1971).

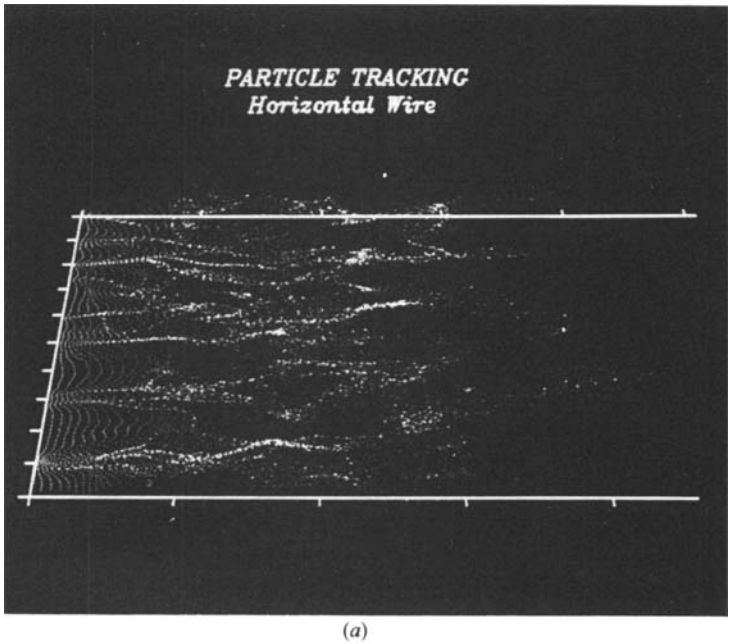

(a)

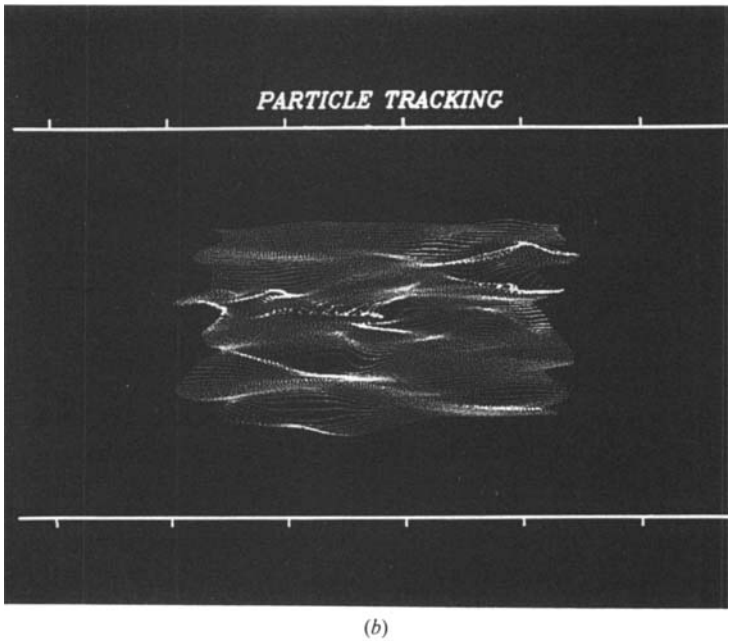

(b)

FIGURE 25(a, b). For caption see facing page.

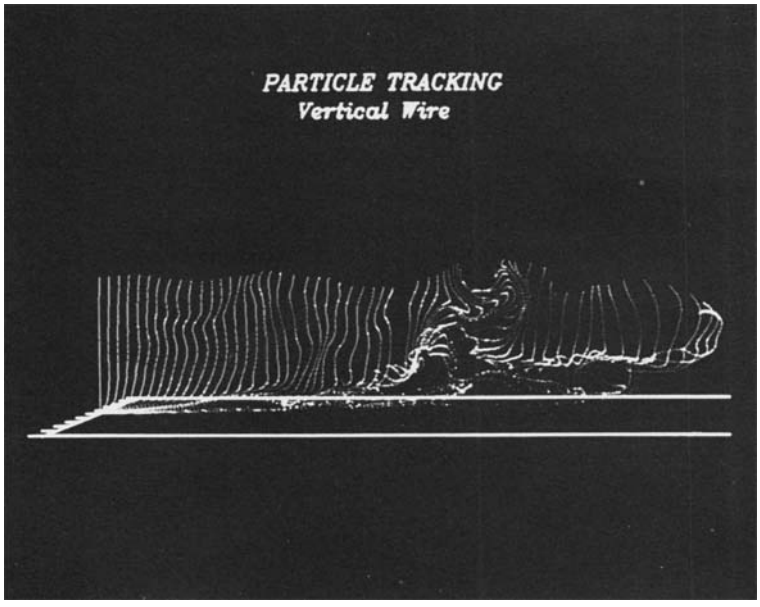

(*c*)

FIGURE 25. Flow structures visualized by fluid markers: (*a*) particles are generated along a line parallel to the z-axis at $y^+ \approx 10$ (oblique top view); (*b*) particles are initially distributed uniformly on a plane parallel to the wall at $y^+ \approx 10$ (top view); (*c*) particles are generated along a line parallel to the y-axis (side view).

6. Summary and discussion

A direct numerical simulation of a turbulent channel flow was carried out with $192 \times 129 \times 160$ mesh points at a Reynolds number of 3300, based on the centreline velocity and channel half-width. A fully spectral method – Fourier series in the homogeneous directions and Chebychev polynomial expansion in the normal direction – is used for the spatial derivatives in conjunction with a second-order time-advancement scheme.

The computed results are compared with experimental results at comparably low Reynolds numbers (most of which were obtained from the oil channel at the Max-Planck-Institut für Strömungsforschung of Göttingen, West Germany). Although the general characteristics of the computed turbulence statistics are in good agreement with the experimental results, detailed comparison in the wall region reveals consistent discrepancies. In particular, the computed Reynolds stresses – both the normal and the shear stresses – are consistently lower than the measured values, while the computed vorticity fluctuations at the wall are higher than the experimental values. The same conclusion was drawn from the other two recent numerical simulations (Moser & Moin 1984; Spalart 1985).

One source of the discrepancy might be related to the measurement of the wall-shear velocity u_τ. When the mean-velocity profiles are renormalized with the corrected (experimental) u_τ, excellent agreement among the experimental results and the computed results is obtained. When the turbulence intensities and the Reynolds shear stress are similarly rescaled, the overall agreement is better, but the computed turbulence intensities, except the streamwise fluctuations, remain lower than the

measured values. Whether or not the remaining differences are due to the cross-contamination mentioned by Perry *et al.* (1985) remains to be resolved. Furthermore, new measurements by J. H. Hartonidis & A. V. Johansson (1985, private communication) indicate that measurements near the wall might be significantly affected by the heat-conduction problem experienced by hot-film probes used to measure the turbulence quantities in the proximity of the wall.

Another source of the discrepancy may be the test section of the oil channel used in the aforementioned experiments. The test section is 22 cm wide and 7 m long, and is filled with oil to a depth of 85 cm, which gives an aspect ratio of 3.9 (depth to width), and the length of the test section is 32 channel widths. This aspect ratio is well below the recommended minimum value of 7 to be representative of 'two-dimensional' flow (Dean 1978). In addition, it is not possible in general that a fully developed state can be reached over such a short length (Comte-Bellot 1963; Hussain & Reynolds 1975). Dean & Bradshaw (1976) pointed out that the mean velocity and turbulence intensities near the centreline overshoot their fully developed values in the developing section. On the other hand, experimental results of Comte-Bellot indicated that the turbulence intensities increased monotonically as the flow develops downstream without any overshoot. Eckelmann (1974) reported that the mean-velocity profiles were independent of streamwise locations, and the variation of the higher-order turbulence statistics (such as skewness and flatness factors of u and v) upstream of the measuring station was within his measurement accuracy; and he concluded that the flow was fully developed.

Although the disagreement between the computed and measured values does not seem to be serious – especially because most disagreements are confined to the immediate vicinity of the wall – it is important to resolve the differences if the use of the computer-generated databases or experimental data in studying turbulence structures and in developing improved turbulence models is to be continued. We hope more thorough investigations will be carried out in the near future to clarify the discrepancies discussed here.

We are grateful to Drs R. S. Rogallo and R. V. Westphal for helpful comments on a draft of this manuscript, and to Dr N. Mansour for numerous discussions we had during the course of this work.

REFERENCES

Alfredsson, P. H. & Johansson, A. V. 1984 On the detection of turbulence-generating events. *J. Fluid Mech.* **139**, 325.

Barlow, R. S. & Johnston, J. P. 1985 Structure of turbulent boundary layers on a concave surface. *Rep.* MD-47, Department of Mechanical Engineering, Stanford University, Stanford, California, USA.

Brodkey, R. S., Wallace, J. M. & Eckelmann, H. 1974 Some properties of truncated turbulence signals in bounded shear flows. *J. Fluid Mech.* **63**, 209.

Chapman, D. R. & Kuhn, G. D. 1984 Computational models of the viscous sublayer and limiting behaviour of turbulence near a wall. *NEAR TR* 334, Nielsen Engineering & Research, Inc., Mountain View, California, USA.

Clark, J. A. 1968 A study of incompressible turbulent boundary layers in channel flow. *Trans. ASME* D: *J. Basic Engng* **90**, 455.

Comte-Bellot, G. 1963 Contribution a l'étude de la turbulence de conduite. Doctoral thesis, University of Grenoble, France.

Dean, R. B. 1978 Reynolds number dependence of skin friction and other bulk flow variables in two-dimensional rectangular duct flow. *Trans. ASME* I: *J. Fluids Engng* **100**, 215.

DEAN, R. B. & BRADSHAW, P. 1976 Measurements of interacting turbulent shear layers in a duct. *J. Fluid Mech.* **78**, 641.

DEARDORFF, J. W. 1970 A numerical study of three-dimensional turbulent channel flow at large Reynolds number. *J. Fluid Mech.* **41**, 453.

ECKELMANN, H. 1970 *Mitteilungen aus dem MPI für Strömungsforschung und der AVA, Göttingen, no.* 48.

ECKELMANN, H. 1974 The structure of the viscous sublayer and the adjacent wall region in a turbulent channel flow. *J. Fluid Mech.* **65**, 439.

FALCO, R. E. 1980 The production of turbulence near a wall. *AIAA Paper* 80-1356.

FINNICUM, D. S. & HANRATTY, T. J. 1985 Turbulent normal velocity fluctuations close to a wall. *Phys. Fluids* **28**, 1654.

GOTTLIEB, D. & ORSZAG, S. A. 1977 *Numerical Analysis of Spectral Methods: Theory and Applications.* CBMS-NSF, Society for Industrial and Applied Mathematics. Philadelphia, PA, USA.

GUPTA, A. K. & KAPLAN, R. E. 1972 Statistical characteristics of Reynolds stress in a turbulent boundary layer. *Phys. Fluids* **15**, 981.

HANJALIC, K. & LAUNDER, B. E. 1976 Contribution towards a Reynolds-stress closure for low-Reynolds-number turbulence. *J. Fluid Mech.* **74**, 593.

HANRATTY, T. J., CHORN, L. G. & HATZIAVRAMIDIS, D. T. 1977 Turbulent fluctuations in the viscous wall region for Newtonian and drag reducing fluids. *Phys. Fluids* **20**, S112.

HINZE, J. O. 1975 *Turbulence*, 2nd edn, p. 621. McGraw-Hill.

HUSSAIN, A. K. M. F. & REYNOLDS, W. C. 1975 Measurements in fully developed turbulent channel flow. *Trans. ASME* I: *J. Fluids Engng* **97**, 568.

JOHANSSON, A. V. & ALFREDSSON, P. H. 1982 On the structure of turbulent channel flow. *J. Fluid Mech.* **122**, 295.

JOHANSSON, A. V. & ALFREDSSON, P. H. 1983 Effects of imperfect spatial resolution on measurement of wall-bounded turbulent shear flows. *J. Fluid Mech.* **137**, 409.

KASTRINAKIS, E. G. & ECKELMANN, H. 1983 Measurement of streamwise vorticity fluctuations in a turbulent channel flow. *J. Fluid Mech.* **137**, 165.

KIM, J. 1983 On the structure of wall-bounded turbulent flows. *Phys. Fluids* **26**, 2088.

KIM, J. 1985 Turbulence structures associated with the bursting event. *Phys. Fluids* **28**, 52.

KIM, J. & MOIN, P. 1985 The structure of the vorticity field in turbulent channel flow. Part 2. Study of ensemble-averaged fields. *J. Fluid Mech.* **162**, 339.

KIM, H. T., KLINE, S. J. & REYNOLDS, W. C. 1971 The production of turbulence near a smooth wall in a turbulent boundary layer. *J. Fluid Mech.* **50**, 133.

KREPLIN, H. & ECKELMANN, H. 1979 Behavior of the three fluctuating velocity components in the wall region of a turbulent channel flow. *Phys. Fluids* **22**, 1233.

LANCZOS, C. 1956 *Applied Analysis.* Prentice-Hall.

LAUFER, J. 1951 Investigation of turbulent flow in a two-dimensional channel. *NACA Rep.* 1053.

LEONARD, A. & WRAY, A. A. 1982 A numerical method for the simulation of three-dimensional flow in a pipe. *Proc. 8th Intl Conf. on Numerical Methods in Fluid Dynamics, Aachen, Germany, 28 June–2 July, 1982*, pp. 335–342. Springer.

MOIN, P. 1984 Probing turbulence via large eddy simulation. *AIAA Paper* 84-0174.

MOIN, P. & KIM, J. 1980 On the numerical solution of time-dependent viscous incompressible fluid flows involving solid boundaries. *J. Comp. Phys.* **35**, 381.

MOIN, P. & KIM, J. 1982 Numerical investigation of turbulent channel flow. *J. Fluid Mech.* **118**, 341.

MOIN, P. & KIM, J. 1985 The structure of the vorticity field in turbulent channel flow. Part 1. Analysis of instantaneous fields and statistical correlations. *J. Fluid Mech.* **155**, 441.

MOSER, R. D. & MOIN, P. 1984 Direct numerical simulation of curved turbulent channel flow. *NASA TM* 85974. Also, *Rep.* TF-20, Department of Mechanical Engineering, Stanford University, Stanford, California, USA.

NIKURADSE, J. 1929 Untersuchungen über die Strömungen des Wassers in konvergenten und divergenten Kanälen. *Forsch. Geb. Ing. Wes.*, Heft 289.

OHJI, M. 1967 Statistical theory of wall turbulence. *Phys. Fluids Suppl.* **10**, S153.

ORSZAG, S. A. & PATERA, A. T. 1981 Subcritical transition to turbulence in planar shear flows. *Proc. Symp. of The Mathematics Research Center, University of Wisconsin-Madison, 13–15 October 1980* (ed. R. E. Meyer), pp. 127–146. Academic.

PERRY, A. E., LIM, K. L. & HENBEST, S. M. 1985 A spectral analysis of smooth flat-plate boundary layers. *Proc. 5th Symp. on Turbulent Shear Flows, 7–9 August 1985, Cornell University, Ithaca, NY*, pp. 9.29–9.34.

REICHARDT, H. 1938 Messungen turbulenter Schwankungen. *Naturwissenschaften*, Jahrg. 26, Heft 24/25, p. 404.

ROGALLO, R. S. & MOIN, P. 1984 Numerical simulation of turbulent flows. *Ann. Rev. Fluid Mech.* **16**, 99.

SABOT, J. & COMTE-BELLOT, G. 1976 Intermittency of coherent structures in the core region of fully developed turbulent pipe flow. *J. Fluid Mech.* **74**, 767.

SCHUMANN, U. 1973 Ein Verfahren zur direkten numerischen Simulation turbulenter Strömungen in Platten- und Ringspaltkanälen und über seine Anwendung zur Untersuchung von Turbulenzmodellen. Dissertation, University of Karlsruhe (NASA Tech. Translation, *NASA TTF* 15391).

SMITH, C. R. & SCHWARTZ, S. P. 1983 Observation of streamwise rotation in the near-wall region of a turbulent boundary layer. *Phys. Fluids* **26**, 641.

SMITH, C. R. & METZLER, S. P. 1983 The characteristics of low-speed streaks in the near-wall region of a turbulent boundary layer. *J. Fluid Mech.* **129**, 27.

SPALART, P. R. 1985 Numerical simulations of boundary layers. *NASA TM* 88220-88222.

TENNEKES, H. & LUMLEY, J. L. 1972 *A First Course in Turbulence*. MIT Press.

WALLACE, J. M., ECKELMANN, H. & BRODKEY, R. S. 1972 The wall region in turbulent shear flow. *J. Fluid Mech.* **54**, 39.

WILLMARTH, W. W. 1975 Pressure fluctuations beneath turbulent boundary layers. *Ann. Rev. Fluid Mech.* **5**, 13.

WILLMARTH, W. W. & LU, S. S. 1972 Structure of the Reynolds stress near the wall. *J. Fluid Mech.* **55**, 65.